



Research papers

Interpretation of glacier mass change within the Upper Yukon Watershed from GRACE using Explainable Automated Machine Learning Algorithms

Cheick Doumbia^{a,*}, Alain N. Rousseau^a, Hakan Başağaoğlu^b, Michel Baraer^c, Debaditya Chakraborty^d

^a Centre Eau Terre Environnement, Institut National de la Recherche Scientifique (INRS), Université du Québec, Québec City, QC, Canada

^b Edwards Aquifer Authority, San Antonio, TX 78215, USA

^c Construction Engineering Department, École de technologie supérieure, Montreal, Quebec, Canada

^d School of Civil and Environmental Engineering, and Construction Management, University of Texas San Antonio, One UTSA Circle, San Antonio, TX, 78249, USA

ARTICLE INFO

This manuscript was handled by Marco Borga, Editor-in-Chief, with the assistance of Di Long, Associate Editor.

Keywords:

Glacier mass temporal variations
Meteorological features
Hydrological features
Explainable machine learning model
Oceanic-climatic oscillations

ABSTRACT

Glaciers play a vital role in providing water resources for drinking, agriculture, and hydro-electricity in many mountainous regions. As global warming progresses, accurately reconstructing long-term glacier mass changes and comprehending their intricate dynamic relationships with environmental variables are imperative for sustaining livelihoods in these regions. This paper presents the use of explainable Machine Learning (XML) models with GRACE and GRACE-FO data to reconstruct long-term monthly glacier mass changes in the Upper Yukon Watershed (UYW), Canada. We utilized the H2O-AutoML regression tools to identify the best performing Machine Learning (ML) model for filling missing data and predicting glacier mass changes from hydroclimatic data. The most accurate predictive model in this study, the Gradient Boosting Machine, coupled with explanatory methods based on SHapley Additive eXplanation (SHAP) and Local Interpretable Model-Agnostic Explanations (LIME) analyses, led to automated XML models. The XML unveiled and ranked key predictors of glacier mass changes in the UYW, indicating a decrease since 2014. Analysis showed decreases in snow water equivalent, soil moisture storage, and albedo, along with increases in rainfall flux and air temperature were the main drivers of glacier mass loss. A probabilistic analysis hinging on these drivers suggested that the influence of the key hydrological features is more critical than the key meteorological features. Examination of climatic oscillations showed that high positive anomalies in sea surface temperature are correlated with rapid depletion in glacier mass and soil moisture, as identified by XML. Integrating H2O-AutoML with SHAP and LIME not only achieved high prediction accuracy but also enhanced the explainability of the underlying hydroclimatic processes of glacier mass change reconstruction from GRACE and GRACE-FO data in the UYW. This automated XML framework is applicable globally, contingent upon sufficient high-quality data for model training and validation.

1. Introduction

Glacier mass balance varies due to spatiotemporal changes in meteorological, physiographical, and environmental conditions (Kinnard et al. 2022; Zhang et al. 2022), with their relationships often exhibiting nonlinearity (Li et al. 2020). Estimating glacier mass changes and elucidating their relationship with driving variables enhance our understanding of the underlying hydroclimatic processes, which is pivotal for climate system monitoring, assessing sea level rise (Arendt et al. 2002; Zemp et al. 2009), enhancing the accuracy of water supply predictions (Yao et al. 2022), as well as calibrating and validating hydrological models (Konz and Seibert 2010), and satellite gravimetry observations (Shean et al. 2020).

Three primary methodological frameworks have been utilized to estimate glacier mass changes: (i) glaciological field techniques surveying; (ii) remote sensing; and (iii) process-based hydrological modeling. Traditional in situ methods provide point measurements such as density, ice thickness, melt rates, and changes in ice-margin elevation (Samuel et al. 2016). These point measurements are then interpolated and extrapolated to generate glacier-scale or regional mass balance estimates (Gardner et al. 2013; Zemp et al. 2019). Remote sensing methods rely on optical, gravity field, and radar data (Gardner et al. 2013; Ciraciet al. 2018; Zhou et al. 2019). For instance, multi-temporal elevation data derived from optical or radar Digital Elevation Models (DEMs) enable geodetic estimates of glacier mass balance

* Corresponding author.

E-mail address: cheick.doumbia@inrs.ca (C. Doumbia).

(Larsen et al. 2015; Zemp et al. 2019; Hugonnet et al. 2021; Jakob et al. 2021). Geodetic methods like time-variable gravity measurements from the Gravity Recovery And Climate Experiment (GRACE) and GRACE Follow-On (GRACE-FO) missions (Chen et al. 2006; Farinotti et al. 2015; Castellazzi et al. 2018; Doumbia et al. 2020) and phase difference analyses from Interferometric Synthetic Aperture Radar (InSAR) datasets also contribute to glacier mass balance assessments (Zhou et al. 2019). Hydrological models have been widely used to estimate glacier mass changes, often utilizing either energy balance methods (which calculate melt from energy fluxes) or temperature-index methods (which rely on the positive correlation between melt rate and positive cumulative air temperature) (Stahl et al. 2008; Rounce et al. 2020).

Estimating regional glacier mass changes is challenging due to the scarcity of in situ data and the inherent limitations of remote sensing techniques. The interpolation of sparse in situ measurements can introduce significant uncertainties in mass balance estimates (Singh et al. 2011). Geodetic methods based on elevation changes can also suffer from temporal sparsity and depict larger uncertainties at shorter timescales (less than 5-year period) (Larsen et al. 2015; Hugonnet et al. 2021). InSAR data, while valuable, can be affected by decorrelation due to significant changes in phase difference between radar images, which can arise from factors such as temporal or spatial baseline shifts, atmospheric conditions, or surface properties. The accuracy of hydrological models is often limited by the availability and quality of data required for model calibration and validation (Stahl et al. 2008; Huss and Hock 2015; Ashokkumar and Harig 2020). On the other hand, GRACE data offers high temporal resolution (10 days to monthly) and a long-time span (over 15 years), but its applicability at regional or watershed scales is constrained by its low spatial resolution (300–400 km) (Baghdadi and Zribi 2016). For hydrological applications, the spatial resolution of GRACE data is around 63,000 km² when considering errors of approximately 2 cm in Equivalent Water Height (Vishwakarma et al. 2018). Ciraciet al.(2020) demonstrated the reliability of using monthly GRACE mission data, along with its successors, and GRACE-FO data with mascon approach to estimate glacier and ice caps mass changes worldwide, except for peripheral glaciers of Antarctica and Greenland. Doumbia et al.(2020) demonstrated that ice mass change dominates GRACE signal over the Gulf of Alaska (GOA) and highlighted the reliability of using the mascon solution from NASA GSFC to estimate glacier mass changes over the Saint Elias Mountains. The results from the latter study highlight the effectiveness of using GRACE MASCON data to estimate regional glacier mass changes over the GOA.

GRACE and GRACE-FO missions, led by United States (NASA) and the German (DLR) space agencies, have been providing changes in Terrestrial Water Storage (TWS) since 2002. The changes are integrated vertically and presented in the form of anomalies (TWSA). TWSAs are derived with respect to variations in the Earth's long-term mean gravity field (Scanlon et al. 2019). The GRACE TWSA consists of various water storage components such as changes in surface water storage, comprising rivers, lakes, reservoirs, canopy, and wetlands, as well as changes in snow cover storage, soil moisture storage, ice storage, and in ground water (Castellazzi et al. 2018, 2019; Doumbia et al. 2020). The GRACE (04/2002–06/2017) and GRACE-FO (06/2018–present) missions, integrated into glaciers geodetic remote sensing (RS) space-borne methods, have been used to estimate glacier mass balance (Gardner et al. 2013; Farinotti et al. 2015; Ciraciet al. 2018; Castellazzi et al. 2019; Ciraciet al. 2020; Tamisiea et al. 2005; Chen et al. 2006; Arendt et al. 2008; Luthcke et al. 2008; Arendt et al. 2009, 2013; Baur et al. 2013; Beamer et al. 2016; Wahr et al. 2016; Jin et al. 2017; Doumbia et al. 2020). Over the GOA, Doumbia et al. (2020) highlighted the reliability of using the inversion method to estimate glacier mass loss over an area of 30,000 km². However, this previous study primarily focused on the GRACE timeframe from 04/2002 to 06/2017 because of the data gap between GRACE and GRACE-FO. Meanwhile, various

methods have been used to reconstruct long-term TWS data from GRACE and GRACE-FO data and fill the 1-year gap (from 06/2017 to 06/2018) between these two datasets. While imputation methods, such as linear or spline interpolation, have been used to fill missing data over periods of one to two months, these methods have shown limitations in predicting missing data over a year (Sun et al. 2021; Wei et al. 2021). Traditional interpolation methods estimate missing values by filling gaps between known values in a time series of predictand. Conversely, Machine Learning (ML) models predict missing data points by learning the relationships between the predictors and the predictand from a complete training dataset. Chakraborty et al. (2021b) demonstrated that traditional interpolation techniques are ill-suited for imputing long stretches of missing data (e.g., 1-year of data gap, as in our study), whereas ML-based imputation technique have shown to be robust and reliable for handling such long-term data gaps.

Sun et al. (2021) provided a comprehensive overview of studies on reconstructing GRACE-like TWSA data. They noted a growing trend in the use of ML algorithms to extend datasets, with recent studies focusing on filling long-term data gaps in GRACE data. Wei et al. (2021) demonstrated the effectiveness of Neural Networks (NN) based on Long Short-Term Memory (LSTM) in reconstructing GRACE and GRACE-FO TWSA over the Qaidam basin in Northwest China. Yu et al. (2021) applied three deep-learning algorithms to reconstruct GRACE-like TWSAs over the Canadian landmass, achieving strong predictive performance with mean correlation coefficients of 0.99 and mean root mean squared error (RMSE) of 53 mm for the testing dataset. Li et al. (2020) and Sun et al. (2020) explored various algorithms for GRACE TWSA reconstruction, underscoring the need for using multiple algorithms to achieve good performance across different basins. Additionally, Sun et al. (2021) demonstrated the effectiveness of H2O Automated Machine Learning (H2O-AutoML) in constructing GRACE TWSA datasets over the conterminous U.S. (CONUS), using five different families of algorithms (LeDell and Poirier 2020). Their results revealed that no single algorithm consistently performed well across all grid points within the study area. However, they highlighted that the main advantage of the AutoML workflow, which allows to run various ML models on the same grid or basin, and select the best (i.e., the leader) model, including the stacked ensemble, while accounting for the spatial and temporal variability of hydrological components. The ML-based studies typically adopt either a gridwise or basin-based approach, using meteorological data (e.g., precipitation, air temperature) and hydrological components of a Land Surface Model (LSM) such as Global Land Data Assimilation System (GLDAS) as predictors (Sun et al. 2021; Wei et al. 2021; Sun et al. 2020). Atmospheric circulation factors, including the North Atlantic Oscillation (NAO) and the Multivariate ENSO Index (MEI) (Sun et al. 2021), and the MEI and the Pacific Decadal Oscillation (PDO) (Wei et al. 2021) have also been incorporated as predictors in the formulation of ML-based models. However, none of these studies aimed to reconstruct GRACE/GRACE-FO TWSA components, such as glacier mass changes, nor did they explore the underlying physics in the reconstruction.

In the ML-based framework, traditional feature importance scores identify the most influential features impacting the global model performance in predicting the target variables (e.g., glacier mass changes) but without explicitly accounting for interrelations and interdependencies among the predictors (e.g., hydrological and meteorological variables). In contrast, SHapley Additive exPlanation (SHAP) (Lundberg et al. 2020) and Local Interpretable Model-agnostic Explanations (LIME) (Ribeiro et al. 2016) analyses, which perform better with tree-based ensemble models, rank the features in the order of importance in predicting target variables while explicitly addressing interrelations and interdependencies among the predictors. In addition, they reveal the inflection point of each predictor, above or below which the target variable either increases or decreases (Chakraborty et al. 2021a; 2021b; 2021c). These explanatory methods are designed to offer global and local explanations, thereby providing a framework to improve the explainability

of ML-based decisions by unraveling nonlinear relationships between predictors and target variables (Wei et al. 2024).

Oceanic–atmospheric circulations influence the temporal evolution of hydrological processes in Yukon, Canada. Fleming and Whitfield (2010) analyzed the impacts of Pacific Decadal Oscillation (PDO) and El Niño Southern Oscillation (ENSO) on the surface meteorological signals of British Columbia, Yukon, and Southeast Alaska. They found that higher and lower air temperatures occurred during PDO and ENSO warm and cool phases, respectively. Rousseau et al. (2020) analyzed the seasonal (spring, summer, winter) correlation between oscillation indices and meteorological data over three watersheds of Yukon, encompassing Upper Yukon, Aishihik and Mayo. They used three indices, including Arctic Oscillation (AO), PDO, and the Multivariate ENSO Index (MEI), and found that correlations for air temperature are stronger than for precipitation. Wang et al. (2006) indicated that the effect of PDO is more significant than that of ENSO on low flows in southern Yukon. However, they noted that ENSO modulated the effect of PDO. Fleming et al. (2006) investigated the effects of AO on rivers fed by glacier and snowmelt within eight watersheds located in southern Yukon and British Columbia. They found a positive correlation between the average annual streamflow of rivers fed by glaciers and the AO index. In their study in Garibaldi Provincial Park, situated in the southern Coast Mountains of British Columbia, Koch et al. (2009) indicated that positive and negative phases of PDO coincide with rapid recession and advances of glaciers, respectively. Different studies showed that PDO influences Wolverine and Gulkana Glaciers located in southeast Alaska (Hodge et al. 1998; Hartmann and Wendler 2005). However, since 1989, these oscillations alone are not sufficient to explain the negative net balance trends observed in both glaciers, and the correlation between the winter balance fluctuations and the PDO is weakening (Josberger et al. 2007). Akansha et al. (2021) analyzed the influence of multiple hydroclimatic variables and energy fluxes on glacier mass changes over the Karakoram and Himalayas region from 2002 to 2019. They found that total precipitation and snowfall are highly correlated to glacier mass changes. Studies over glaciers located in Yukon, GOA, and other Canadian glaciers also depicted the effect of hydroclimatic variables and energy fluxes on glacier mass changes (Foy et al. 2011; Samuel et al. 2016; Marshall and Miller 2020; Chesnokova et al. 2020; Kochtitzky et al. 2020; Kinnard et al. 2022). This motivates the inclusion of hydroclimatic variables as predictors in our analyses.

The primary objective of our study is to reconstruct monthly glacier mass changes using the GRACE and GRACE-FO CSR RL06 MASCON TWSA datasets and highlight the relationships between glacier mass changes and various meteorological and hydrological variables within the Upper Yukon Watershed (UYW). Our reconstruction aims to capture long-term glacier mass changes for the period of 2002–2020 and provide insights into the physical processes driving them, using H2O-AutoML algorithms and two explanatory methods (i.e., SHAP and LIME). Additionally, our study investigates the potential impact of climatic oscillations on glacier mass changes, leveraging enhanced explainability of outcomes through XML. To the best of our knowledge, this study represents the first attempt to implement XML-based reconstructed glacier mass changes from GRACE and GRACE-FO data.

2. Study area

The southern and northern parts of the Upper Yukon Watershed (UYW) (~20,000 km²) are in the Canadian province of British Columbia and in Yukon Territory, respectively. Glaciers are predominantly found in high elevations of British Columbia in the southwest and northwest parts of the watershed. According to the Randolph Glacier Inventory (RGI 6.0) dataset (RGI Consortium 2017), the UYW hosts 466 glaciers representing ~ 5% of the watershed area (Fig. 1). Molnia (2008) focused on the glaciers of Alaska and indicated that their areas are divided into two parts separated by the Equilibrium Line Altitudes (ELA). The area covered by snow and firn, located over the highest elevations,

is called accumulation zone, while the ablation area, located over the lowest elevations, is covered by ice (Braithwaite and Raper 2009; Radić et al. 2014; Huss and Hock 2015; Rounce et al. 2020). Based on their fieldwork within the glaciers of UYW, Samuel et al. (2016) observed that snow accumulation starts in late September or early October and snow melt ends completely by the end of May or the middle of June. Over the largest glaciers of UYW, they also found that ice begins to melt in the lowest and highest elevations of the ablation area in the middle of April and at the end of June, respectively. According to the Köppen-Geiger classification, over the period 1991–2020, the UYW had three distinct climate types: BSk (Arid, Steppe, Cold), Dsc (Cold, Dry Summer, Cold Summer), and ET (Polar, Tundra) (Beck et al. 2020).

3. Data and methods

3.1. GRACE and GRACE-FO TWS data

In this study, GRACE and GRACE-FO data were obtained from the non-decomposed regularized CSR RL06 MASCON TWS solution (Save et al. 2016, 2020). Based on the distribution of glacier mass losses reported by Larsen et al. (2015), resampled at the same resolution as CSR RL06 MASCON TWS solution (0.25°), there are six (6) CSR RL06 MASCON pixels corresponding to the glaciers over the UYW (Fig. 2a). The GRACE TWSA consists of various water storage components, including Δ SWS (changes in surface water storage, comprising rivers, lakes, reservoirs, canopy, and wetlands), Δ SS (changes in snow cover storage), Δ SMS (changes in soil moisture storage), Δ IS (changes in ice storage), and Δ GWS (changes in ground water storage). The GRACE signal is affected by the glacial isostatic adjustment (GIA) and Δ GIA represents changes in GIA (Castellazzi et al. 2018, 2019; Doumbia et al. 2020). However, considering the dominance of ice mass changes in the GRACE signal over the GOA, as defined by Doumbia et al. (2020), we used the non-decomposed CSR RL06 MASCON TWS. Our reconstruction process is based on the spatial mean glaciers mass loss from these six CSR RL06 MASCON pixels over GRACE and GRACE-FO periods (2002–2020) (Fig. 2b).

3.2. Reconstruction of GRACE and GRACE-FO glacier mass changes

3.2.1. Data and pre-processing

Numerous studies showed the reliability of using hydroclimatic variables to explore changes in glacier mass. Li et al. (2019) used the annual values and trends in total precipitation and average air temperature to investigate their relationship with glacier mass loss across different regions from 1980 to 2015. They found good correlations between annual meteorological variables (average air temperature and total precipitation) and glacier retreat rates. Hock (2005) emphasized the crucial role of energy fluxes in glacier melt processes. In their study, linear interpolation was applied to fill one- to two-month gaps in the CSR RL06 MASCON GRACE and GRACE-FO TWSA monthly time series data. Based on previous studies and the theoretical relationship between changes in glacier mass and environmental variables (as elaborated in the next paragraph), two types of hydroclimatic predictors were selected, including meteorological (e.g., precipitation) and hydrological (e.g., soil moisture storage) variables. Additional variables representing time (year and month) and the chronological sequence of the monthly data series were included in the predictor list to better capture temporal variations in glacier mass (Table 1).

Hydroclimatic variables from LSM NOAA GLDAS and ERA5-Land have been used in studies focusing on the reconstruction of GRACE and GRACE-FO TWS. Sun et al. (2020) showed that meteorological data from ERA-interim and TWS components (snow water equivalent (SWE) and soil moisture storage (SMS) from 0 to 200 cm) from LSM NOAA GLDAS, chosen as predictors for Deep Neural Network (DNN) algorithms, can provide accurate estimates. Akansha et al. (2021) estimated GLDAS-derived TWS by using Soil Moisture Storage, Snow Water

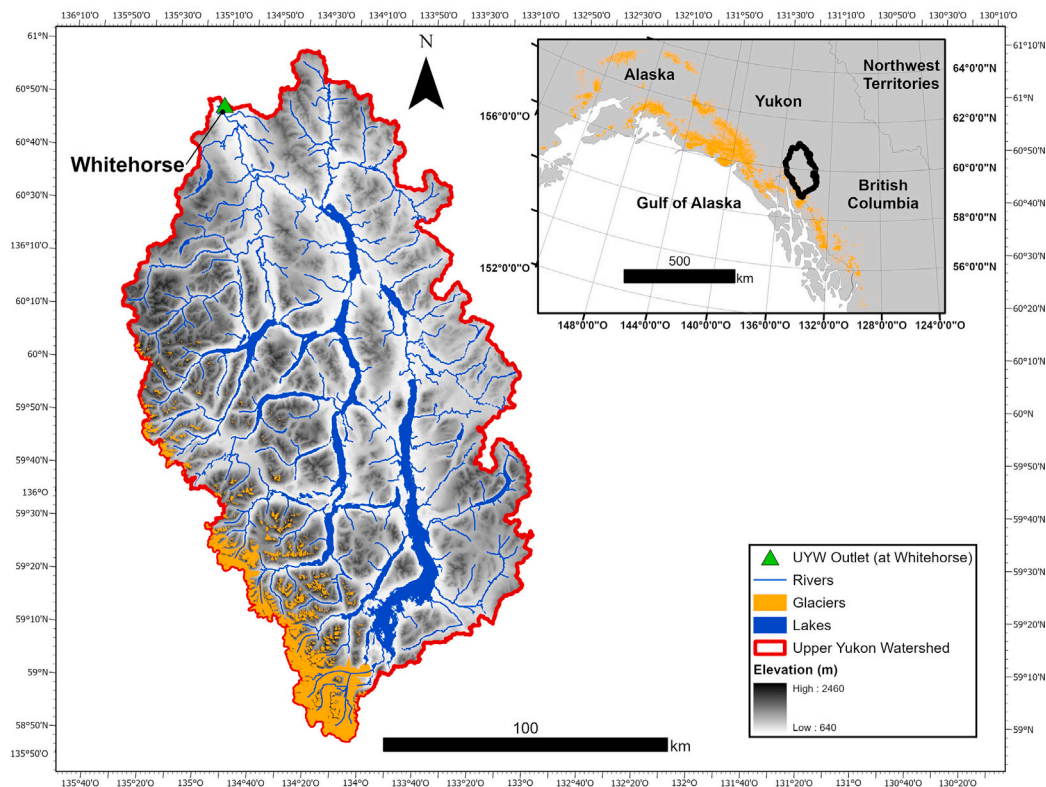


Fig. 1. The Upper Yukon Watershed spans about 20,000 km² and comprises about 5% glacier cover.

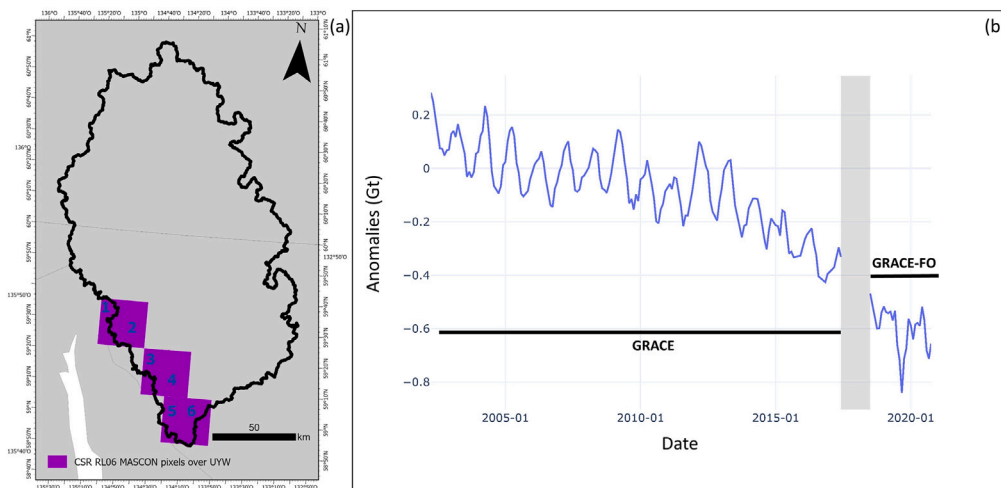


Fig. 2. Glacier mass changes from CSR RL06 MASCON over the UYW for the period 2002–2020. (a) Six (6) CSR RL06 MASCON pixels over the glaciers of UYW, located in the southwestern part; and (b) Spatial mean of the CSR RL06 MASCON monthly TWS changes in Gt from the six pixels over the UYW. The 1-year gap between GRACE and GRACE-FO is shown in gray in (b).

Equivalent, and Canopy Water Storage from monthly GLDAS NOAH land surface model (Version 2.1) with spatial resolution $0.25^\circ \times 0.25^\circ$ from October 2002 to September 2019. They also used total precipitation, snowfall, air temperature, evaporation, total runoff, and energy flux components (i.e., net shortwave and net longwave radiation) from ERA5-Land to analyze the relationship between these variables and glacier mass changes from GRACE and GRACE-FO over the Karakoram and Himalayas region from 2002 to 2019. However, some studies identified biases associated with ERA5-Land data (e.g., precipitation) (Huang et al. 2022; Akinsanola et al. 2024). Sun et al. (2020) showed the reliability of using precipitation and air temperature data from

ERA5-Land, provided in the form of anomalies, along with TWS components from the LSM NOAH GLDAS v2.1 as inputs to drive H2O-AutoML algorithms in GRACE-like TWSA simulations. The hydroclimatic variables used in this study are derived from the sources detailed in these previous studies. To mitigate uncertainties related to ERA5-Land data in mountainous areas, only two monthly meteorological forcing data (i.e., precipitation and air temperature) were obtained from this dataset, which is an improvement of ERA-interim in terms of model, data assimilation system, and both spatial and temporal resolutions (Muñoz 2019) (Table 1). The spatial resolution of this reanalysis is 0.1° . The remaining meteorological forcing and the two hydrological datasets were monthly data from LSM NOAH GLDAS v2.1 with a

Table 1

The predictors used in the Machine Learning model. Note that they are expressed as temporal changes (Δ).

	Predictor	Name	Unit	Source
Temporal components	Series	Monthly sequence	–	–
	Year	Years	Year	–
	Month	Months	Month	–
Meteorological variables	Precip	Total precipitation	m	^a
	Temp	Temperature 2 m above ground surface	°C	^a
	Evap	Water evaporation flux	kg m ⁻² s ⁻¹	^b
	Long_wav	Surface net downward longwave flux	W m ⁻²	^b
	Shor_wav	Surface net downward shortwave flux	W m ⁻²	^b
	Gr_fl	Downward heat flux in soil	W m ⁻²	^b
	H_fl	Surface upward sensible heat flux	W m ⁻²	^b
	lat_fl	Surface upward latent heat flux	W m ⁻²	^b
	R_fl	Rainfall flux	kg m ⁻² s ⁻¹	^b
	Sn_fl	Snowfall flux	kg m ⁻² s ⁻¹	^b
	Alb	Surface albedo	%	^b
Hydrological variables	SMS	Soil moisture storage	cm	^b
	SWE	Snow water equivalent	cm	^b

^a ERA5-Land.

^b LSM NOAA GLDAS v2.1

spatial resolution of 0.25° (Table 1). To ensure compatibility with CSR RL06 MASCON data and adhere to physical interaction principles, the predictors (i.e., meteorological and hydrological variables) underwent several pre-processing steps: meteorological data were collected with a one month-gap preceding glacier mass changes, illustrating the lag time necessary to observe the effects of these variables on glaciers (Sun et al. 2020; Sun et al. 2021); For each of the six(6) CSR RL06 MASCON pixels (0.25°) over the UYW (Fig. 2), data were resampled as monthly spatial means and then long-term means (January 2004 to December 2009) were subtracted from monthly values to obtain anomalies (temporal changes) aligning with CSR MASCON RL06 solution (Eq. (1)).

$$\text{Anomaly} = \text{Monthly value} - \text{Monthly mean over (01/2004 - 12/2009)} \quad (1)$$

3.2.2. H2O-AutoML algorithms

In this study, H2O-AutoML v3.38.0.3 algorithms were used to reconstruct monthly glacier mass changes from CSR RL06 MASCON. H2O-AutoML randomly selects the training and testing data sets (Sun et al. 2021). H2O-AutoML is an open source, fully automated, and distributed engine comprised of six distinct ML algorithm families (Text S1) belonging to supervised learning methods with an emphasis on regression modeling and classification, along with two stacked

ensembles models (Ciabuschi and Venkateswaran 2017; LeDell and Poirier 2020; Sun et al. 2021). The ML algorithm families include Generalized Linear Model (GLM), Deep Neural Network (DNN), Gradient Boosting Machine (GBM), Extreme Gradient Boosting GBM (XGBoost), eXtremely Randomized Trees (XRT), and Distributed Random Forests (DRF). The hyperparameters of each model are provided in Tables S1, S2, and S3. H2O-AutoML automatically performs, pre-processing tasks such as normalization/standardization, and imputation.

To obtain the most reliable model, a random grid-hyperparameter search was performed for each model, and a k-fold (4-fold in our analyses) cross-validation was implemented during the training process of each model. The hyperparameters and their ranges for each model were established on the training data through grid search. The grid search, however, was not performed for RF and XRT. Instead of performing a standard grid search, only the model with the best alpha-lambda combination was selected using a lambda search based on the list of alpha values (Table S1). The training data were used during the k-fold cross-validation. For each algorithm, k-fold cross-validation was applied by training and validating on 80% and 20% of the training data, respectively. Subsequently, the resulting model, chosen by combining the k models, was trained on 100% of the training data, and the evaluation metrics of this combined holdout model were computed. This approach ensures robustness, especially when working with small datasets, like those used in this study. The best model, also referred to as the leader, was automatically selected from the five families of algorithms and the two stacked ensembles, based on evaluation metrics and two methods, including random grid search and k-fold cross-validation. LeDell and Poirier (2020) reported that the grid search and stacking method used by H2O-AutoML yielded excellent results within the same computation time, comparable to more complex tuning methods, such as Bayesian optimization and genetic algorithms.

There are two H2O-AutoML stacked ensembles models: one that includes all models and another composed of the best models from each of the six families (LeDell and Poirier 2020; Sun et al. 2021). According to LeDell and Poirier (2020), the latter stacked ensembles, referred to as ‘best of family’, is more efficient in production as it includes fewer models (i.e., five or less). While it provides faster simulation results than the full ensemble, its performance may be slightly lower. These stacked ensembles are also referred to as Super Learner algorithms due to the use of k-cross validation. An optimal asymptotic system was demonstrated by the two H2O-AutoML stacked ensembles models. Fig. 3 provides a summary of the approach used to reconstruct the monthly glacier mass changes using H2O-AutoML algorithms.

3.2.3. Training process, evaluation metrics, and validation

The random 4-fold cross-validation was used during the training process to fine-tune the hyperparameters. The process involved four main steps: (i) splitting the data into training and testing sets; (ii) fine-tuning hyperparameters on the training data; (iii) identifying performance metrics for both cross-validation data and training data; and (iv) selecting performance metrics for the leader model. Sun et al. (2021) obtained relevant results from H2O-AutoML using an 85% training and 15% testing data split. In this study, considering all available data (i.e., GRACE and GRACE-FO), the splitting was adjusted to 75% training and 25% for testing. To prevent overfitting, several parameters were defined for the training process: the maximum time was set to 8 h; the maximum number of models to 25; the default stopping metric based on deviance or mean squared error and stopping tolerance based on the number of rows (i.e., instance or months).

The leader model was automatically chosen based on the evaluation metrics. For H2O-AutoML, the performance metrics included the coefficient of determination (R^2), mean squared error (MSE, Eq. S1), root mean squared error (RMSE, Eq. S2), root mean squared logarithmic error (RMSLE, Eq. S3), and mean absolute error (MAE, Eq. S4) for the cross-validation and training datasets.

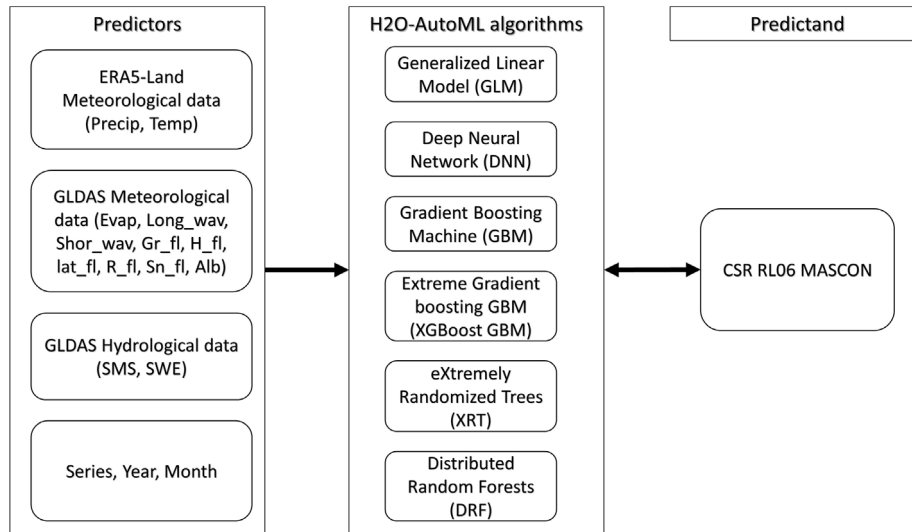


Fig. 3. A building block of the H2O-AutoML model. The first panel on the left lists all predictors, including hydroclimatic variables associated with meteorological features, hydrological features, and temporal features such as years, months, and chronological series. The names and units of these predictors are provided in Table 1. The second panel in the middle lists the H2O-AutoML algorithm families used in the analysis. The last panel on the right shows the monthly GRACE CSR RL06 MASCON glacier mass changes, which serve as the target variable in the analysis.

The predictive performance of the leader model, representing the ability of the algorithms to predict glacier mass changes, was evaluated on the test data using normalized RMSE (NRMSE), Nash–Sutcliffe efficiency (NSE), correlation coefficient (CC), and percent bias (Pbias). The NRMSE is the RMSE (Eq. (2)) normalized by the mean of observed data, providing a measure of the global performance of the model. It ranges from 0 to ∞ with the best performance corresponding to 0 (Eq. (3)). The NSE is a normalized statistic parameter, measuring the predictive efficiency of a model by estimating the relative amplitude of the residual variance in comparison to the variance in the observed data. It ranges from $-\infty$ to 1, with 1 corresponding to the best fit (Nash and Sutcliffe 1970) (Eq. (4)). The CC quantifies the linear correlation between observed and simulated values. It ranges from -1 to 1, with the best correlation corresponding to 1 (Eq. (5)). The Pbias (in %) estimates the goodness of a model by measuring the average tendency of the simulated data to be larger or smaller than the corresponding observed data (Eq. (6)). The optimal value is 0, with positive and negative values corresponding to overestimation and underestimation biases of the model, respectively (Gupta et al. 1999).

$$RMSE = \sqrt{\frac{\sum_{i=1}^n (y_i - \hat{y}_i)^2}{n}}, \quad (2)$$

$$NRMSE = \frac{RMSE}{\bar{y}}, \quad (3)$$

$$NSE = 1 - \frac{\sum_{i=1}^n (y_i - \hat{y}_i)^2}{\sum_{i=1}^n (y_i - \bar{y})^2}, \quad (4)$$

$$CC = \frac{\sum_{i=1}^n (y_i - \bar{y})(\hat{y}_i - \bar{\hat{y}})}{(\sum_{i=1}^n (y_i - \bar{y})^2)^{1/2} (\sum_{i=1}^n (\hat{y}_i - \bar{\hat{y}})^2)^{1/2}}, \quad (5)$$

$$Pbias = 100 \times \frac{\sum_{i=1}^n (\bar{y} - y_i)}{\sum_{i=1}^n y_i}, \quad (6)$$

where y is the variable, y_i is the i th observation of y , \hat{y}_i is the i th predicted value of y , \bar{y} is the mean of observation of y , and $\bar{\hat{y}}$ is the mean of predicted value of y .

3.2.4. Comparison of reconstructed glacier mass changes with data from Hugonnet et al. (2021)

To assess the reliability of the reconstructed glacier mass changes from this study, we compared the decadal values with those reported by Hugonnet et al. (2021). Our reconstruction is based on the average mass variations of glaciers within $0.25^\circ \times 0.25^\circ$ grid cells, at the scale

of the UYW. This reconstruction covers the period from 04/01/2002 to 10/01/2020, aligning with the start date of GRACE data, which begins on 04/01/2002. The data from Hugonnet et al. (2021) consists of a trend map at a resolution of $0.5^\circ \times 0.5^\circ$, covering a longer period from 01/01/2000 to 01/01/2020. To facilitate a comparison, we downscaled the data from Hugonnet et al. (2021) to a resolution of $0.25^\circ \times 0.25^\circ$ at the scale of the UYW, by considering the proportions of glacier areas within the smaller and larger grid cells. The average glacier mass losses were then calculated for the UYW based on these downscaled grid cells. We compared our estimates, which cover the period from 01/01/2003 to 01/01/2020, with the data from Hugonnet et al. (2021) for the extended period from 01/01/2000 to 01/01/2020.

The trend in glacier mass changes from our reconstruction was derived using a method applied in earlier studies (Castellazzi et al. 2018, 2019; Ciraciet al. 2018, 2020; Doumbia et al. 2020). This involved implementation of a 13-month moving average filter to reduce the influence of seasonal fluctuations, followed by a linear regression fitting on the smoothed monthly data time series to obtain the trend slope, representing glacier mass changes from 01/01/2002 to 01/01/2020.

3.2.5. Interpretation of the ML algorithms and explanation of the results

ML models are often viewed as black boxes, lacking transparency in revealing the underlying relationships between predictors and target variables. To overcome this limitation, SHAP analysis, built on the game theory approach, and LIME analysis are commonly used to elucidate the non-linear relationships between predictors and predictands (Zhi et al. 2024). The integration of SHAP and LIME into ML modeling framework is commonly referred to as eXplainable Machine Learning (XML) (Chakraborty et al. 2021b). XML facilitates the explanation of predicted values for each instance by establishing causal connections between predictands and real-world physical processes. This capability enhances the explainability and transparency of results from ML models, allowing users to understand the underlying reasoning (Ribeiro et al. 2016; Chakraborty et al. 2021b; Dikshit and Pradhan 2021; Ryo 2022). The primary advantage of SHAP and LIME analyses, in comparison to the traditional statistical or sensitivity analysis, is their ability to explicitly consider the interdependency and interaction among the predictors in predicting target variables (Bařaęaoęlu et al. 2021). Lundberg et al. (2020) demonstrated that SHAP analysis provides enhanced explanatory when used with tree-based ensemble models. Global SHAP explanations, shown by beeswarm plots, unveils

Table 2
The reconstruction performance of the models from H2O-AutoML.

AI-Model		NSE	NMRES	CC	Pbias
GBM	Training	0.99	0.01	0.99	0
	Testing	0.97	0.04	0.98	-7.9
Stack ensemble best of family	Training	0.99	0.01	0.99	0.63
	Testing	0.96	0.04	0.98	-8.07
Stack ensemble all models	Training	0.99	0.01	0.99	0.12
	Testing	0.97	0.04	0.99	-8.29
DNN	Training	0.98	0.03	0.99	5.08
	Testing	0.93	0.06	0.97	-7.14
XRT	Training	0.99	0.02	0.99	-0.24
	Testing	0.95	0.05	0.98	-8.36
DRF	Training	0.99	0.02	0.99	0.02
	Testing	0.95	0.05	0.98	-9.07
GLM	Training	0.88	0	0.94	0.08
	Testing	0.80	0.1	0.9	-13.20

the order of importance of predictors in predicting the target variables. In addition, local explanations for each predictor, displayed as dependence plots, identify inflection point of each predictor above/below which the target variables vary positively or negatively in response to the changes in the value of a predictor (Başgaoglu et al. 2021). In addition, LIME analysis supplies local interpretation, providing explanations for individual predictions, and can be interfaced with various ML algorithms (Ribeiro et al. 2016; Lundberg et al. 2019; Chakraborty et al. 2021ba). In this study, beeswarm plots, dependence plots, and local explanation based-individual predictions are used to explain the reconstructed glacier mass changes by the best H2O-AutoML model.

3.2.6. Conditional probabilistic analysis

Using the inflection point identified through the local SHAP analysis, we established specific meteorological and hydrological conditions associated with global mass changes. These conditions describe how glacier mass loss in the UYW may increase if a predictive value falls below or exceeds its inflection point. The combined effects of these conditions on glacier mass loss can be analyzed using the conditional probabilistic analysis

$$P(C_i \cup C_j | C_0) = 100 \times \frac{P(C_i \cap C_0) \cup P(C_j \cap C_0)}{P(C_0)}\%, \quad (7)$$

where C_i and C_j represent the specific conditions based on the inflection points, and C_0 represent the target condition. This analysis quantifies the percent contributions of meteorological and hydrological factors to glacier mass loss.

3.3. Oceanic-climatic oscillations

PDO and ENSO strongly influence air temperature (Fleming and Whitfield 2010; Rousseau et al. 2020), and warm phases of PDO induce glacial melt (Neal et al. 2002; Koch et al. 2009). Regarding the theoretically strong relation between air temperature and glacier mass changes and the impact of PDO on glaciers, indices from both oscillations can be used to investigate their role in the temporal changes of the reconstructed glacier mass and to unveil nuanced interpretation from XML. In this study, we used the PDO index from the National Centers for Environmental Information (PDO NCEI), and two ENSO indices, namely Niño 3.4 index and Oceanic Niño Index (ONI). These three indices are monthly data based on the extended reconstruction of sea surface temperature (ERSST Version 5; Huang et al. (2017)) from the National Oceanic and Atmospheric Administration (NOAA). Available online,¹ they represent the average changes (i.e., anomalies)

of SSTs across specific regions. PDO is the leading pattern of SSTs changes from the empirical orthogonal function (EOF) in the North Pacific region. Niño 3.4 index and ONI are the average of SSTs changes within 5N-5S, 170W-120 W and are defined according to 5-month and 3-month running mean, respectively. For Niño 3.4 index, El Niño or La Niña events are defined when temporal changes of SSTs exceed +0.4 °C and -0.4 °C for a period of six months or more. For ONI, El Niño or La Niña events are defined when changes of SSTs exceed +0.5 °C and -0.5 °C for at least five consecutive months.

4. Results and discussion

4.1. Reconstruction of monthly glacier mass change

One of the primary advantages of using an AutoML tool is its ability to select the best ML model from a range of available options. In this study, the Gradient Boosting Machine (GBM) emerged as the best predictive model within the H2O-AutoML family. (Table S4). Fig. 4 and Table 2 illustrate the predictive reconstruction performance of the GBM model, in comparison to other models. The model adeptly reconstructs monthly glacier mass changes from CSR RL06 MASCON over the UYW from 2002 to 2020 (Fig. 4).

Fig. 5 shows that the long-term glacier mass change estimated in this study, $-37.20 \text{ Mt/yr}/0.25^\circ \times 0.25^\circ$, is in close agreement with $-33.05 \text{ Mt/yr}/0.25^\circ \times 0.25^\circ$ reported by Hugonnet et al. (2021). Wang et al. (2021) noted that similarity in long term glacier mass changes from different sources indicates consistency in the estimates. Thus, the results indicate that the glacier mass changes estimates from this study are reliable. As explained in Section 1 and Section 3.2.4, our comparison spans a longer period (01/01/2002–01/01/2020 and 01/01/2000–01/01/2020) to avoid larger uncertainties identified over shorter timescales (less than 5-year period) by Hugonnet et al. (2021). A statistical test is applied in Section 3.3 to the reconstructed glacier mass changes to identify trend breakpoints.

4.2. Global SHAP explanation

Because GBM is a tree-based model, it is well-suited for coupling with SHAP. The Shapley value represents the average marginal contribution of each predictor value across all possible combinations of predictors. Predictors with large absolute Shapley values are deemed important in accurately predicting the target variables. The global explanation from SHAP, as depicted by beeswarm plot in Fig. 6, identifies the most influential features, ranked by importance, for accurately predicting glacier mass changes. In this figure, the importance of the predictors is presented in descending order, with the most influential predictors listed at the top. Hot-colored and cold-colored dots correspond to the high and low predictor values, respectively. Positive and negative of SHAP values on the x-axis correspond to glacier mass gain and loss, respectively. For example, larger increases, as defined by Eq. (1), in snow water equivalent (ΔSWE), depicted by red dots, are associated with glacier mass gain, as indicated by positive SHAP values on the x-axis. Conversely, more recent years, denoted by red dots, are associated with glacier loss, as indicated by negative SHAP values on the x-axis.

Global SHAP analysis in Fig. 6 unveils that years, temporal changes in snow water equivalent, soil moisture storage, and surface albedo, along with months and changes in rainfall flux and air temperature are the most critical features in the order of importance in predicting glacier mass changes in the study region. Among them, later years and months, in addition to larger increases in rainfall flux and air temperature are associated with higher glacier mass loss (i.e., positive feedback); larger increases in snow water equivalent, soil moisture storage, and surface albedo are associated with higher glacier mass gain (i.e., negative feedback).

¹ <https://www.ncei.noaa.gov/access/monitoring/products/>.

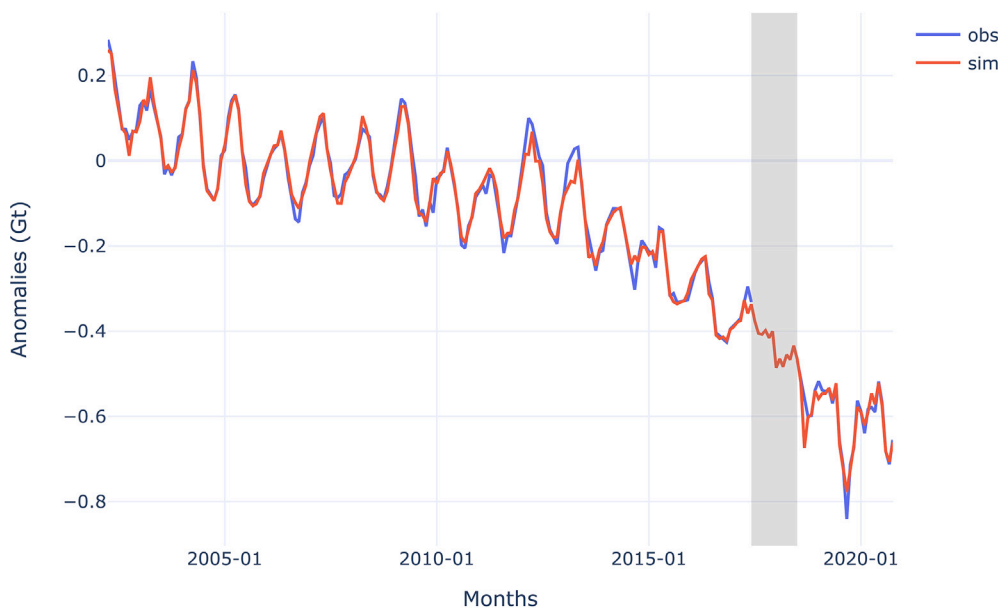


Fig. 4. The reconstruction of the spatial mean glacier mass changes over the UYW using H2O-AutoML algorithms for the period of 04/2002-10/2020. ‘obs’ represents monthly glacier mass changes from CSR RL06 MASCON and ‘sim’ represents monthly glacier mass changes reconstructed. The gray band represents the one-year gap between GRACE and GRACE-FO.

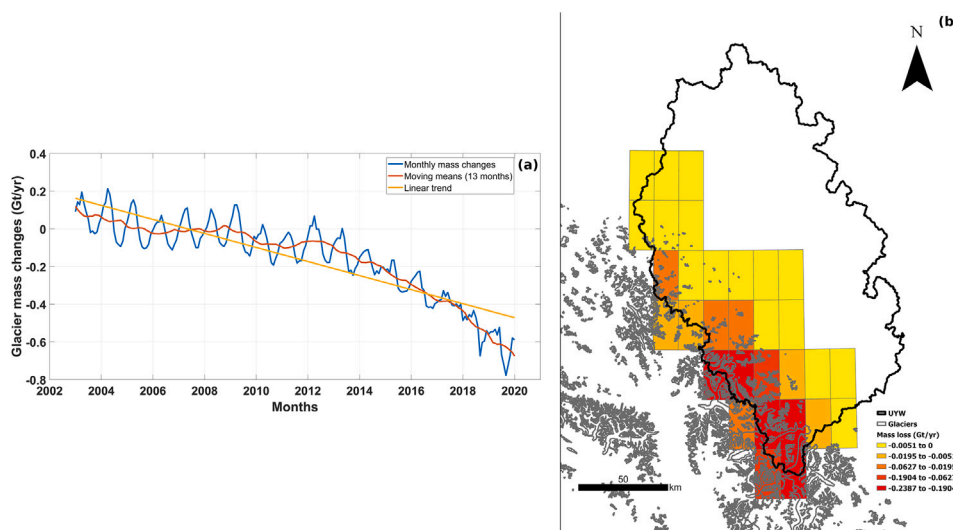


Fig. 5. Comparison of average glacier mass changes on $0.25^{\circ} \times 0.25^{\circ}$ grid cells, within the UYW. (a) Reconstructed glacier mass changes from GBM over the UYW, from 01/01/2003 to 01/01/2020; (b) Glacier mass changes from Hugonnet et al. (2021) within the UYW, from 01/01/2000 to 01/01/2020.

Oerlemans (2005) related changes in air temperature to changes in glacier length from 169 glacier records. Yao et al. (2012) discovered regional difference in glacier evolution in Tibetan Plateau due to different patterns in air temperature, precipitation, and atmospheric circulation. Mölg et al. (2014) showed that precipitation conditions from May to June, influenced by both mid-latitude dynamics and the onset of intensity of Indian summer monsoon, largely determine the annual mass balance of Zhadang Glacier on the southern Tibetan Plateau from 2001 to 2011. Global SHAP analysis in Fig. 6 revealed that while changes in air temperature are critical for glacier mass changes in the UYW, changes in precipitation is relatively less influential. Although the effects of oceanic-climatic oscillation indices on the hydroclimatic processes have been studied for the UYW, there is a lack of field and associated analyses on the impacts of the most critical hydroclimatic features in Fig. 6, including Δ SWE, Δ SMS, Δ Alb, and Δ R_{fl}. This gap will be addressed in the subsequent sections using XML modeling analysis;

however, these results need to be validated with field data in future studies.

4.3. Local SHAP explanation

The local SHAP explanation provides a broader overview of the influence from the most important features and unfolds nonlinear relationship between predictors and target variables (Fig. 7). The local analysis hinges on the inflection point, through which it reveals how the value of the target variable changes with changes in the predictor value above or below its inflection point. The inflection point of the predictor is determined from the x-axis for the SHAP curve, where it takes a zero value on the y-axis, corresponding to the transition from glacier mass gain (associated with positive SHAP values) to glacier mass loss (associated with negative SHAP values) (Chakraborty et al. 2021a, 2021b). In local SHAP plots, hot-colored and cold-colored dots represent the magnitude of a predictor, with hot-colored dots

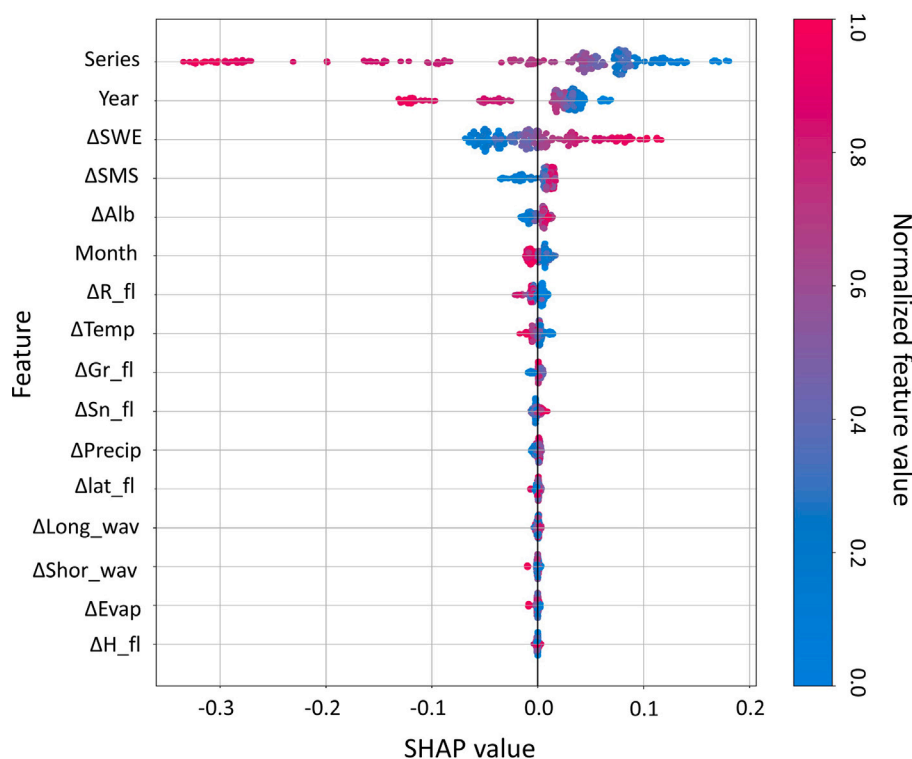


Fig. 6. The global explanation from GBM-SHAP for glacier mass changes from 2002 to 2020 over the UYW (please refer to Table 1 for explanations of the acronyms). (For interpretation of the references to color in this figure legend, the reader is referred to the web version of this article.)

indicating larger values and blue dots indicating smaller values. Hot-colored dots with positive SHAP values show that glacier mass increases as the predictor value exceeds its inflection point. Conversely, cold-colored dots with negative SHAP values indicate that glacier mass decreases as the predictor value falls below its inflection point.

The local SHAP analysis associated with the GBM model in Fig. 7a-b reveals that glacier mass in the UYW region has been decreasing since June 2014. We analyzed the reconstructed glacier mass changes depicted in Fig. 4 using the statistical Chow test (Pancotto et al. 2024). This analysis identified five trend breakpoints: July 2004, July 2009, August 2013, July 2016 and January 2018 (Fig. 8a). The breakpoint of August 2013 is aligned with the inflection point displayed on Fig. 7a, indicating that glacier mass loss has accelerated since 2014. The year 2014 marks the shift in the magnitude of larger negative glacier mass in Fig. 4. Moreover, mass loss predominantly occurs in August through December, while glacier mass accumulation is observed from January through May. On the other hand, LIME analysis revealed that glacier mass loss largely occurred from June through October (Figure S2). In their global study on the impact of future glacier mass loss on hydrology, Huss and Hock (2018) considered that the glacier melt season over the Northern Hemisphere spanned from June to October. Additionally, using the hydrological model CHRM over the Peyto Glacier Research Basin (i.e., a glacierized headwater basin in the Canadian Rockies) over the period 2000–2015, Aubry-Wake and Pomeroy (2023) showed that glacier melt occurred from June to October. These observations are consistent with the explanation provided by LIME, highlighting the importance of using different explanatory methods and comparing their outcomes to ensure the reliability of analyses.

In Fig. 7c, an increase in glacier mass is evident when changes in SWE ≥ -0.76 cm, whereas mass decreases when the snow cover exists in low quantities. This phenomenon, well-observed and documented in earlier studies (e.g., Samuel et al. 2016), is analogous to the definition of the ELA. Indeed, theoretically, the zone of glaciers gaining mass (accumulation zone) is covered by snow, firn and/or ice, while the ablation area is covered by ice during the ablation season. Foy

et al. (2011) analyzed changes in volume and surface area of the Kaskawulsh Glacier, Yukon. They observed prominent thinning of this glacier throughout the ablation zone, while the accumulation zone exhibited relative stability and even slight thickening since 1995.

Fig. S1 further illustrates that increases in glacier mass predominantly occurred during the years prior to 2014 when changes in SMS < 2.17 cm. Additionally, in Fig. 7d, soil moisture drying conditions, represented by changes in SMS < -2.17 cm, are associated with glacier mass loss, while soil moistening conditions, represented by changes in SMS ≥ -2.17 cm, are linked with glacial mass accumulation. According to Aubry-Wake and Pomeroy (2023), soil moisture storage increases from mid-May to July before decreasing until October. Armstrong and Brun (2008) noted the regional cooling effect from moist spring soils. The increase and the associated cooling effect from spring soil moisture could explain the glacier mass loss associated with the increase in SMS depicted by the local SHAP analysis. Indeed, this cooling effect can create a micro-climate, extending the snow cover season and delaying the onset of the ice melt season. However, due to the difficulty in establishing the casual-effect relationship between soil moisture and glacier mass changes, further studies are needed to establish their interaction (Section 4.6).

Fig. 7e unveils that when changes in Alb $\geq 2.39\%$, it fosters glacier mass accumulation, whereas changes in Alb $< 2.39\%$ may lead to ablation. This feedback from albedo on glacier mass changes aligns with the basic land surface thermal energy balance principles. Kinnard et al. (2022) showed that the reduction in albedo serves as an important driver of warming, influencing the mass balance of the Saskatchewan Glacier. In their study on the seasonal evolution and interannual variability of snow and ice albedo at Haig Glacier located in Canadian Rocky Mountains, Marshall and Miller (2020) found a strong negative correlation between monthly mean albedo and monthly melt, with a Pearson correlation coefficient of -0.88 from 2002 to 2015. Figs. S3–S5 show that albedo is influenced by air temperature, and precipitation phases (Rainfall and Snowfall); Fig. S3 depicts the decrease of albedo with an increase in air temperature; Fig. S4 shows an increase in

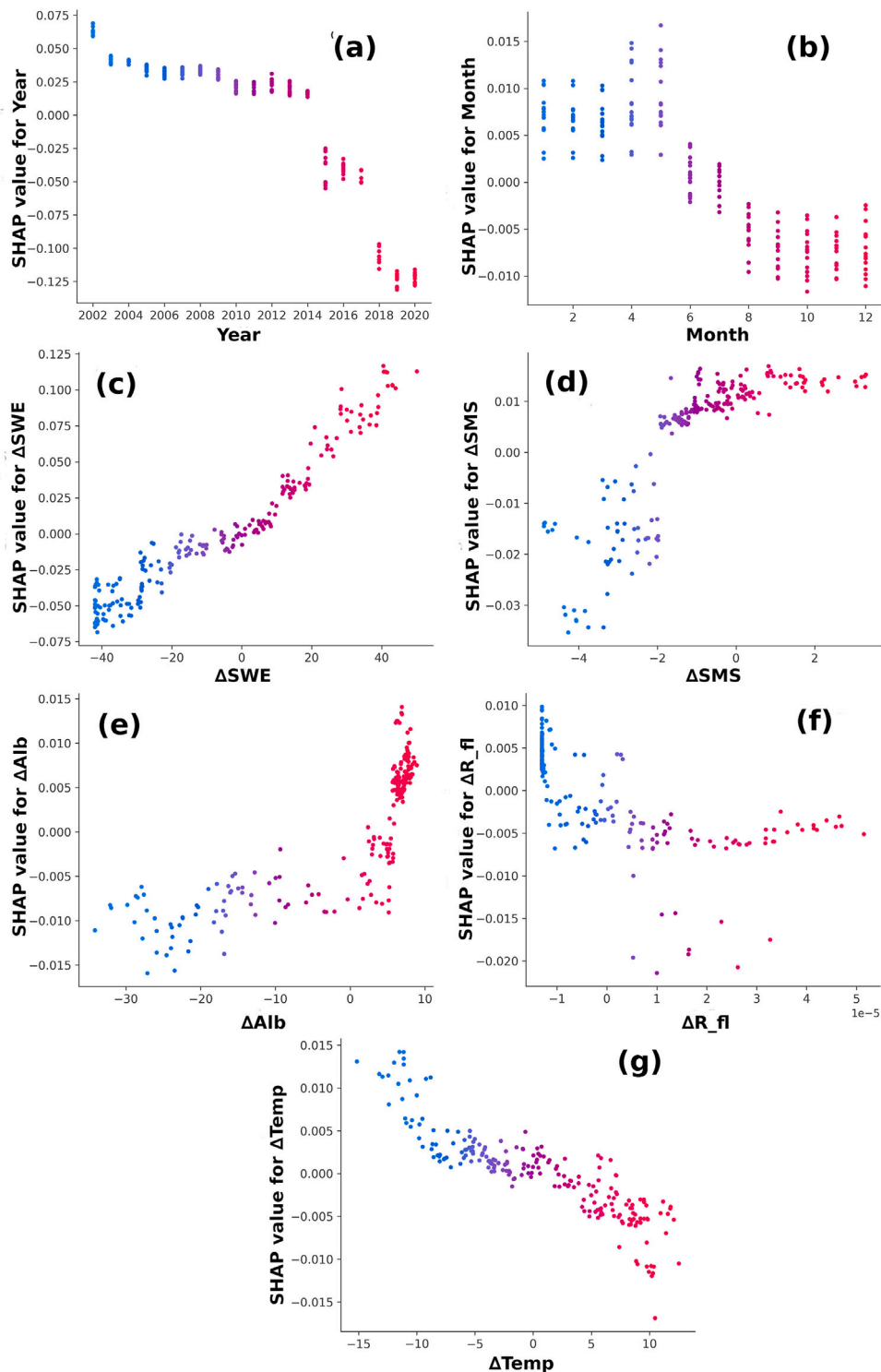


Fig. 7. Local explanation of most critical predictors from GBM-SHAP in predicting glaciers mass changes over the UYW. (a) years (Year); (b) months (Month); (c) changes in snow water equivalent (Δ SWE) in cm; (d) changes in soil moisture storage (Δ SMS) in cm; (e) changes in surface albedo (Δ Alb) in %; (f) changes in rain flux in (Δ R_fl) $\text{kg m}^{-2} \text{s}^{-1}$; (g) air temperature (Δ Temp) in $^{\circ}\text{C}$. (For interpretation of the references to colour in this figure legend, the reader is referred to the web version of this article.)

albedo with a decrease in rainfall flux; and Fig. S5 depicts decrease in albedo with a decrease in snowfall flux. These relationships were well illustrated by Kinnard et al. (2022).

Moreover, in Fig. 7f, changes in $R_{fl} \geq -1.2 \times 10^{-5} \text{ kg m}^{-2} \text{ s}^{-1}$ results in glacier mass loss. The positive feedback from rainfall flux was demonstrated by Roy et al. (2024) on the Chorabari glacier located in the Upper Ganga Basin, Central Himalaya, India. Kinnard et al. (2022)

showed that warming, which leads to glacier loss, alters precipitation phase by increasing rainfall. Chesnokova et al. (2020) analyzed the glacier retreat and the associated hydrological changes in eight watersheds in the Southwestern Yukon. Their analysis of data from two meteorological stations near our study area, Atlin (673.6 m a.s.l., 1967–2017, 1967–2018) and Teslin (705.0 m a.s.l., 1944–1994, 1944–2018), revealed no change in mean annual precipitation at Atlin and an increase

in precipitation at Teslin. The air temperature effects in Fig. 7g indicate that changes in Temp < 0.6 °C create favorable conditions for glacier mass accumulation. The near 0 °C inflection point is well-established in glaciological studies and commonly used hydrological modeling (Hock 2005). Thus, negative and positive changes in air temperature correspond to glacier mass accumulation and ablation, respectively. In their study on surging of Donjek Glacier, Yukon, Kochtitzky et al. (2020) showed that increase in air temperature corresponds to negative glacier mass balance. Chesnokova et al. (2020) found an increase in air temperature at the Atlin and Teslin stations, which are located near the UYW.

4.4. Probabilistic analysis

We formulated a probabilistic model (Stef et al. 2023) to analyze how potential changes in the topmost critical predictors, identified by the global SHAP analysis in Fig. 6, could drive glacier mass loss in the UYW. Based on the inflection points, determined by the local SHAP analysis in Fig. 7 and the reconstructed glacier mass changes (Fig. 4), we first set the following conditions:

- C_0 : Glacier mass depletion \geq Median Glacier mass depletion,
- C_1 : $\Delta\text{Temp} \geq 0.6$ °C,
- C_2 : $\Delta\text{SWE} < -0.76$ cm,
- C_3 : $\Delta\text{SMS} < -2.17$ cm,
- C_4 : $\Delta\text{Alb} < 2.39\%$,
- C_5 : $\Delta\text{R_fl} \geq -1.2 \times 10^{-5}$ kgm⁻²s⁻¹,

where $C_0 - C_5$ represent the labels for different conditions used in the probabilistic analysis. Specifically, C_0 represents the target condition, which is the glacier mass depletion, to be explored probabilistically with median glacier mass change equal to 0 Gt. C_1 , C_4 , and C_5 account for the impact of the critical meteorological forcings, and C_2 and C_3 represent the impacts of the critical hydrological forcings on the glacier mass depletion. A conditional probability for the occurrence of specific conditions $C_1 - C_5$ in relation to C_0 can be expressed as:

$$P(C_2 \cup C_3 | C_0) = 100 \times \frac{P(C_2 \cap C_0) \cup P(C_3 \cap C_0)}{P(C_0)} \%, \quad (8)$$

$$P(C_1 \cup C_4 \cup C_5 | C_0) = 100 \times \frac{P(C_1 \cap C_0) \cup P(C_4 \cap C_0) \cup P(C_5 \cap C_0)}{P(C_0)} \%, \quad (9)$$

where $P(C_i \cap C_0)$ is the probability that C_i and C_0 concurrently occur. $P(C_0)$ represents the probability of glacier mass depletion being higher than the median glacier mass depletion for the period of 2002 to 2022. $P(C_0) = 50\%$ serves as the baseline for the probabilistic analysis. $P(C_i | C_0)$ represents the probability of further depletion in glacier mass beyond the baseline case when C_i occurs. Thus, Eq. (8) quantifies the reduction in glacier mass beyond the baseline case under unfavorable hydrological conditions. Similarly, Eq. (9) quantifies the additional depletion in glacier mass beyond the baseline case due to unfavorable meteorological conditions. Using, Eqs (8)–(9), we obtained:

$$P(C_2 \cup C_3 | C_0) = 100\%; P(C_1 \cup C_4 \cup C_5 | C_0) = 73\%.$$

Given the baseline values of 50%, these results indicate that the hydrological and meteorological forcings could lead to 100.0% and 73% (62.6% from Temp, ERA5-Land data and 73.3% from Alb and R_fl LSM NOAA GLDAS data according to the baseline values of 50%) reduction in glacier mass, respectively. These findings suggest that the hydrological forcings are more critical than the meteorological forcings in glacier mass balance assessments and predictions at the UYW.

Given the significance of consistency across different explanatory methods, as indicated in the feedback analysis from the predictor Month, we compare local explanation outcomes from SHAP and LIME for the months of August through October to ensure the reliability of the results. Both methods consistently identified glacier mass loss during these months.

Table 3

Retro-actions or feedbacks from key predictors, in terms of changes, on August, September, and October from SHAP and LIME for each year over the period 2002–2020. (–) feedback denotes glacier mass accumulation, while (+) feedback denotes glacier mass depletion. Specific conditions based on individual years for the variables ‘Year’ and ‘ ΔSMS ’ are provided.

	August		September		October	
	SHAP	LIME	SHAP	LIME	SHAP	LIME
Year	(–) <2015 (+) ≥ 2015	(–) <2016 (+) ≥ 2016	(–) <2015 (+) ≥ 2015	(–) <2016 (+) ≥ 2016	(–) <2015 (+) ≥ 2015	(–) <2016 (+) ≥ 2016
ΔSWE	(+)	(+)	(+)	(+)	(+)	(+)
ΔSMS	(–) $\neq 2016$, 2019	(–) $\neq 2016$, 2019	(–) $\neq 2013$, [2015–20]	(–) $\neq 2010, 2013$, [2015–19]	(–) $\neq 2013$, [2015–20]	(–) $\neq [2013–20]$
ΔAlb	(+)	(+)	(+)	(+)	(+)	(+)
Month	(+)	(+)	(+)	(+)	(+)	(+)
$\Delta\text{R_fl}$	(+)	(+)	(+)	(+)	(+)	(+)
ΔTemp	(+)	(+)	(+)	(+)	(+)	(+)

4.5. Interpretation based on key physical features during the months with high glacier mass losses

LIME and SHAP facilitate the analyses of the positive or negative effects of predictors on glacier mass changes for each month. Both methods presented predictor values and their effect on glacier mass changes. LIME provided enhanced precision by identifying the necessary threshold or range values required for specific positive or negative impacts. Additionally, LIME was capable of categorizing predictors according to their importance in influencing glacier mass changes, prioritizing those with the most substantial impact.

In this section, local explanations from both methods were compared to assess the agreement of important physical features during months with high glacier mass losses, specifically August, September, and October (Table 3; Figs. S6–S8). For each of these three months in each year, the SHAP analysis unveiled that glacier mass losses increased in 2015, while LIME depicted this increase started from 2016. This observation aligns with the findings discussed in Section 4.3, specifically referencing to August 2013. The SHAP and LIME analyses showed positive feedbacks from ΔSWE , ΔAlb , Month, $\Delta\text{R_fl}$, and ΔTemp . The feedbacks from SMS were generally negative during the initial years (2002 to 2013, as reported in Table 3). However, differences emerged in the years of ΔSMS ’s positive feedbacks for the two months, September and October (Table 3). Specifically, in September, SHAP revealed positive feedbacks in 2013 and throughout the period of 2015–2020, while LIME indicated positive feedbacks in 2010, 2013 and from 2015 to 2019. Similarly, in October, SHAP showed positive feedbacks in 2013 and from 2015 to 2020, while LIME showed positive feedbacks from 2013 to 2020. In summary, SHAP and LIME exhibited good agreement in depicting the feedbacks from the key predictors on glacier mass changes, with some difference in the predictor Year and ΔSMS (Table 3). Such differences from SHAP and LIME analyses are expected due to their differences in methodology and consistency. From a methodological standpoint, LIME perturbs the input data and trains local interpretable models to approximate the behavior of the original model near a specific prediction. The method can be sensitive to the choice of perturbation and the local model’s complexity, which might lead to variations in results. On the other hand, SHAP uses game theory to calculate the exact contribution of each feature to a prediction, providing a globally consistent explanation based on Shapley values (see Table 3).

The similarity between explanations from SHAP and LIME analyses indicates that both methods are capable of extracting reliable relationships between physical predictors and glacier mass changes.

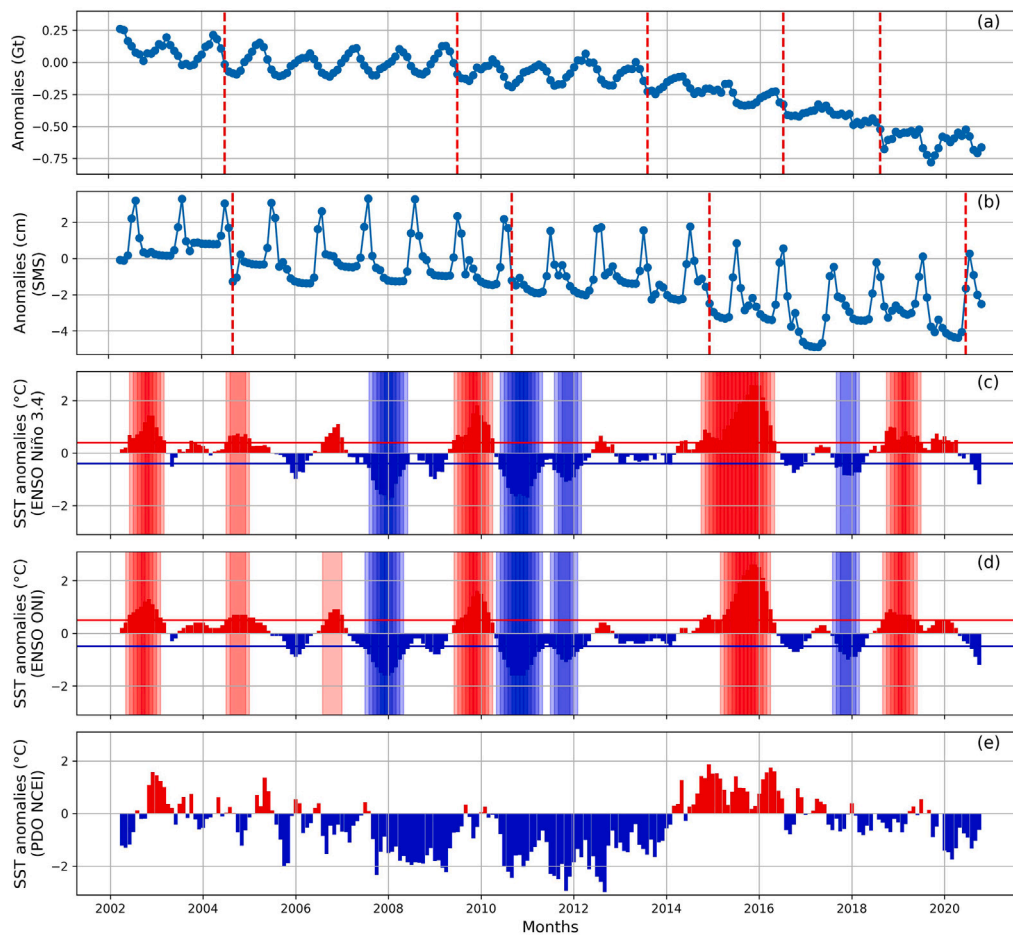


Fig. 8. Indirect evidence for the relationships between changes in normalized glacier mass balance and Δ SMS. (a) changes in glacier mass; (b) changes in SMS; (c) SST changes associated with the El Niño-Southern Oscillation ENSO Niño 3.4 where El Niño (red band) and La Niña (blue band) events are defined based on the threshold of $+0.4$ °C (horizontal red line) and -0.4 °C (horizontal blue line); (d) El Niño-Southern Oscillation Oceanic Niño Index, ENSO ONI where El Niño (red band) or La Niña (blue band) events are defined based on the threshold of $+0.5$ °C (horizontal red line) and -0.5 °C (horizontal blue line); and (e) Pacific Decadal Oscillation National Centers for Environmental Information, PDO NCEI. (For interpretation of the references to color in this figure legend, the reader is referred to the web version of this article.)

4.6. Indirect evidence of the relationship between changes in soil moisture storage and glacier mass

Figs. 6 and 7d unveiled that changes in glacier mass are positively and nonlinearly related to Δ SMS. However, there is a lack of compelling field data to corroborate this finding. To further scrutinize the validity of such a relationship, we examined the impacts of SST changes, a surrogate measure reflecting changes in climatic conditions, on changes in glacier mass depletion and SMS. Niño 3.4 index reveals that El Niño events were observed in 2002–2003, 2004–2005, 2009–2010, 2014–2016, 2018–2019 (Fig. 8c). ONI also depicts similar pattern with Niño 3.4 index but its longest El Niño event, covering the period 2015–2016, was shorter (Fig. 8d). The longest positive phase of PDO NCEI was observed from 2014 to 2016 (Fig. 7e). There was rapid depletion in glacier mass in July 2004, July 2009, August 2013, July 2016, and January 2018 (Fig. 8a). The rapid depletion in soil moisture changes was observed in September 2004, September 2010, December 2014, and June 2020 (Fig. 8b). According to these results, both glacier mass change and Δ SMS exhibit similar responses to increases in SST (positive phase for PDO NCEI, and El Niño events for Niño 3.4 index and ONI), resulting in significant depletion in both glacier mass and SMS starting from 2014 (Fig. 8). This significant depletion is well identified by the XML in SHAP and LIME local explanations (Sections 4.3 and 4.5). This result is corroborated by previous studies showing that positive phases or conditions of oscillations indices coincide with rapid recession of glaciers (Fleming et al. 2006; Koch et al. 2009).

These results indicate a strong correlation between changes in SSTs and glacier mass as well as changes in SSTs and SMS. They also unveil an indirect evidence for the correlative relationship between changes in glacier mass and SMS. Furthermore, the power spectral density analysis in Fig. 9a illustrates that changes in glacier mass and SMS share common underlying dynamics and patterns, but at different scales, with changes in SMS exhibiting higher amplitudes (Fig. 9). Additionally, the cross-correlation in Fig. 9b indicates robust correlations within a 6-month time window between changes in SMS and glacier mass in response to SST fluctuations, with $R^2 > 0.9$. This 6-month time window aligns closely with the El Niño events, which correspond to the periods of six months or more and the periods of at least five consecutive months with changes of SSTs exceeding $+0.4$ °C and $+0.5$ °C for Niño 3.4 index and ONI, respectively.

4.7. Limitations and uncertainties

The observed difference of approximately 10% between the multidecadal glacier mass changes from this study and those reported by Hugonnet et al. (2021) can be attributed primarily to variations in data sources, inherent uncertainties, and post-processing methods. Hugonnet et al. (2021) estimated glacier mass changes using Digital Elevation Models and identified density conversion as a major source of uncertainty due to its poor estimation. While initially CSR RL06 mascon solutions are represented at a $0.25^\circ \times 0.25^\circ$ resolution, their current native resolution is $1^\circ \times 1^\circ$ (Save et al. 2016, 2020). In

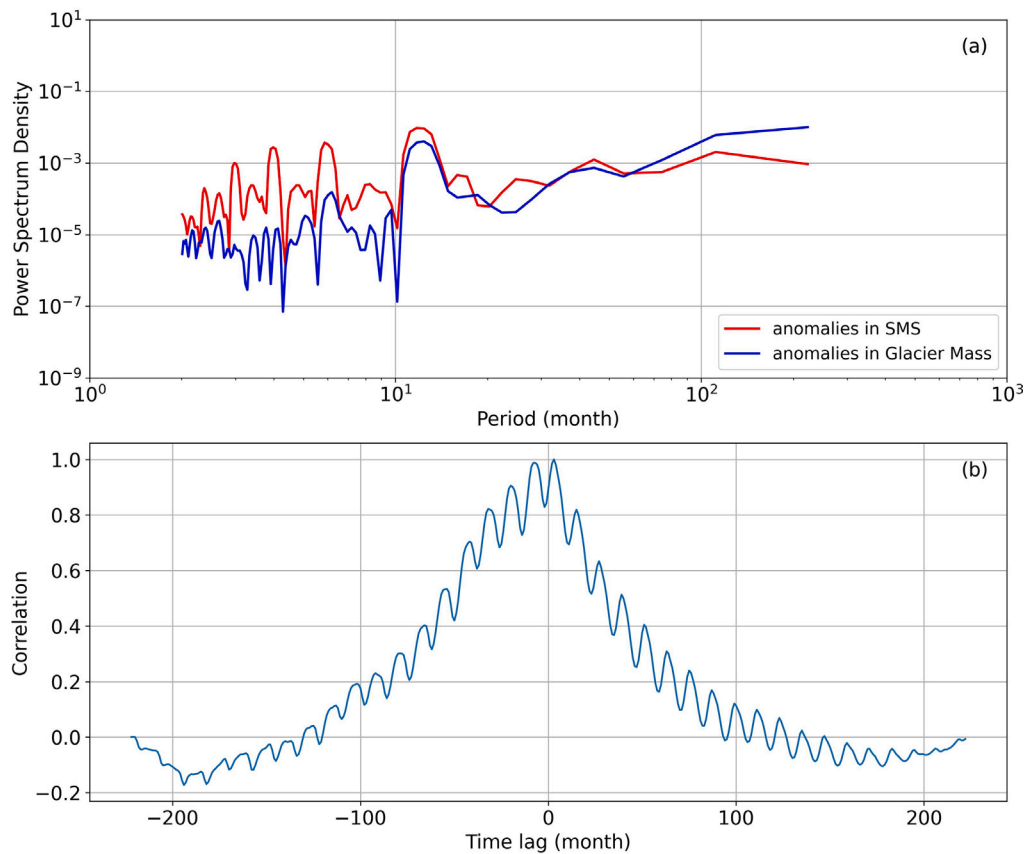


Fig. 9. Comparison of normalized changes in glacier mass and Δ SMS in the frequency domain. The original, non-normalized, plots are given in Figure S8. (a) Power spectrum densities of glacier mass and Δ SMS; and (b) cross-correlation between changes in glacier mass and Δ SMS.

this study, the CSR RL06 MASCON TWS solution was resampled to match $0.25^\circ \times 0.25^\circ$ grid used for the distribution of glacier mass losses reported by Larsen et al. (2015). Our analyses are based on the fact that GRACE signal, consisting of various water storage components, is largely dominated by ice mass change over the GOA (Doumbia et al. 2020). Thus, the use of CSR RL06 MASCON solution at high resolution without subtracting other water storage components may introduce uncertainties, which could explain the observed differences. However, the similarity in glacier mass changes from CSR RL06 MASCON and data from Hugonnet et al. (2021) suggest that resampling to a 0.25° -pixel of CSR RL06 MASCON reduce resolution-related uncertainties and effectively capture the temporal relationship between glacier mass changes and hydroclimatic variables. Additional uncertainties may arise from the use of LSM NOAA GLDAS and ERA5-Land data used as predictors.

One of the main limitations of this study is the lack of comprehensive research studies and field data on the factors influencing the evolution of glacier mass in the study area. This is particularly evident in understanding the interaction between soil moisture and glaciers, which we explored based on indirect evidence in Section 4.6. Additionally, the variables used in this study were chosen based on previous studies and our theoretical understanding of glacier mass evolution. Fortunately, this latter limitation is alleviated by identifying the most critical variables through the SHAP analysis. Under various circumstances, the recognition that the variables used are not independent of each other could influence the selection of topmost critical variables. However, the SHAP analysis takes into account interactions and interdependencies among predictors, notably through local SHAP explanations. Furthermore, comparing the results from the SHAP and LIME analyses helps reduce estimation uncertainties.

5. Conclusions

This study aimed to reconstruct glacier mass changes over the UYW by filling the 1-year data gap between GRACE and GRACE-FO CSR RL06 MASCON data, spanning from 2002 to 2022. The objective was to unveil the importance, and interdependencies and interrelations among physics-based processes behind this reconstruction.

To achieve this, GRACE-like glacier mass changes were reconstructed using six families of algorithms and two stacked ensembles from H2O-AutoML. The predictive performance of the H2O-AutoML algorithms was evaluated using standard performance metrics, such as NSE, Pbias, NRMSE, and CC. The best ML algorithm identified from H2O-AutoML platform was the GBM, illustrating the importance of using different algorithms to analyze glacier mass changes over a watershed. On the testing set, encompassing 25% of the dataset, the GBM exhibited decent predictive performance with NSE of 0.97, Pbias of 8%, NRMSE of 0.04 and CC of 0.98. The explanatory methods SHAP and LIME were used to reveal the key variables through global explanatory analysis and their inflection points using local explanatory analysis in the reconstruction process using the GBM model. In addition, probabilistic analysis was used to determine percent contributions of key predictors to glacier mass losses. Finally, oceanic-climatic oscillation indices were used to analyze the changes in glacier mass and to investigate the relationship between changes in glacier mass and soil moisture.

Global explanation from SHAP highlighted the importance and global influence of predictors in the reconstruction process using the GBM model. Key predictors were identified, including temporal sequence indicators and energy and water balances components, such as years, months, changes in snow water equivalent, soil moisture storage, surface albedo, changes in rainfall flux, in addition to air

temperature. Local explanations identified the inflection (critical) point of each key predictor. These points are instrumental in illustrating how glacier mass change with the changes in the values of key predictors above or below their inflection point. The inflection points also provided the foundation for establishing probabilistic analyses to quantify the contribution of key predictors to variations in glacier mass. The theoretical physics-based relationships between glacier mass changes and the key predictors were well-captured. The probabilistic analysis further revealed that the hydrological conditions are more critical than the meteorological conditions in glacier mass balance assessments and projections. The LIME explanation provided more precise estimates for the predictor Month on glacier mass changes compared to SHAP. Both SHAP and LIME local explanations provided further insights into the physical processes behind glacier mass reductions. While both methods revealed similar effect from the most important features, discrepancies were observed in Year and SMS. These local explanations underscored the reliability of using different explanatory methods to comprehend the glacier mass depletion process over the UYW. The analysis of oceanic-climatic oscillation indices revealed their direct influence on glacier mass changes and provided evidence for correlations with both glacier mass changes and Δ SMS.

Abbreviations

Commonly used symbols and abbreviations in the paper:

Δ	Anomalies (Temporal Changes)
CC	Correlation Coefficient
CSR	Center for Space Research
EOF	Empirical Orthogonal Function
ERSST	Extended Reconstruction of SSTs
GBM	Gradient Boosting Machine
GIA	Glacial Isostatic Adjustment
GOA	Gulf Of Alaska
GRACE	Gravity Recovery And Climate Experiment
GRACE-FO	Gravity Recovery And Climate Experiment Follow-On
GRGS	Space Geodesy Research Group
GWS	Ground Water Storage
H2O-Auto ML	H2O Automated Machine Learning
IS	Ice Storage
LIME	Local Interpretable Model-agnostic Explanations
LSTM	Long Short-Term Memory
NOAA	National Oceanic and Atmospheric Administration
NRMSE	Normalized Root Mean Squared Error
NSE	Nash–Sutcliffe Efficiency
ONI	Oceanic Niño Index
Pbias	Percentage of Bias
PDO	Pacific Decadal Oscillation
NCEI	National Center for Environmental Information
RMSE	Root Mean Squared Error
R^2	Coefficient of determination
SHAP	SHapley Additive Explanation
SS	Snow Cover Storage
SST	Sea Surface Temperature
SMS	Soil Moisture Storage
SWE	Snow Water Equivalent
SWS	Surface Water Storage
TWS	Terrestrial Water Storage
TWSA	Terrestrial Water Storage Anomalies
UYW	Upper Yukon Watershed
XML	eXplainable Machine Learning

CRediT authorship contribution statement

Chieck Doumbia: Writing – review & editing, Writing – original draft, Visualization, Methodology, Formal analysis, Data curation, Conceptualization. **Alain N. Rousseau:** Writing – review & editing, Writing – original draft, Supervision, Methodology, Funding acquisition, Conceptualization. **Hakan Başağaoğlu:** Writing – review & editing, Methodology, Formal analysis. **Michel Baraer:** Writing – review & editing, Supervision, Conceptualization. **Debaditya Chakraborty:** Writing – review & editing, Methodology, Formal analysis.

Declaration of competing interest

The authors declare that they have no known competing financial interests or personal relationships that could have appeared to influence the work reported in this paper.

Acknowledgments

The authors wish to gratefully acknowledge the financial support of the Natural Sciences and Engineering Research Council of Canada, Canada (NSERC) and the Yukon Energy Corporation (YEC), Canada for this research. The authors gratefully acknowledge the contribution of Romain Hugonnet (University of Washington) who provided glacier mass change data over UYW. The authors would also like to thank Stephen Déry of the University of Northern British Columbia for his useful comments on an earlier interpretation of our results.

Appendix A. Supplementary data

Supplementary material related to this article can be found online at <https://doi.org/10.1016/j.jhydrol.2024.132519>.

Data availability

Data will be made available on request.

References

- Akansha, Patel, Ajanta, Goswami, Jaydeo, K. Dharpure, Meloth, Thamban, Anil, V. Kulkarni, Parmanand, Sharma, 2021. Regional mass variations and its sensitivity to climate drivers over glaciers of Karakoram and Himalayas. *GIScience Remote Sens.* 58 (5), 670–692. <http://dx.doi.org/10.1080/15481603.2021.1930730>.
- Akinsanola, A.A., Jung, C., Wang, J., Kotamarthi, V.R., 2024. Evaluation of precipitation across the contiguous United States, Alaska, and Puerto Rico in multi-decadal convection-permitting simulations. *Sci. Rep.* 14, 1238. <http://dx.doi.org/10.1038/s41598-024-51714-3>.
- Arendt, Anthony A., Echelmeyer, Keith A., Harrison, William D., Lingle, Craig S., Valentine, Virginia B., 2002. Rapid wastage of Alaska glaciers and their contribution to rising sea level. *Science* 297 (5580), 382–386. <http://dx.doi.org/10.1126/science.1072497>.
- Arendt, Anthony, Luthcke, Scott, Gardner, Alex, O’Neel, Shad, Hill, David, Moholdt, Geir, Abdalati, Waleed, 2013. Analysis of a GRACE global mascon solution for Gulf of Alaska glaciers. *J. Glaciol.* 59 (217), 913–924. <http://dx.doi.org/10.3189/2013JoG12J197>.
- Arendt, Anthony A., Luthcke, Scott B., Hock, Regine, 2009. Glacier changes in Alaska: can mass-balance models explain GRACE mascon trends? *Ann. Glaciol.* 50 (50), 148–154. <http://dx.doi.org/10.3189/172756409787769753>.
- Arendt, Anthony A., Luthcke, Scott B., Larsen, Christopher F., Abdalati, Waleed, Krabill, William B., Beedle, Matthew J., 2008. Validation of high-resolution GRACE mascon estimates of glacier mass changes in the St Elias Mountains, Alaska, USA, using aircraft laser altimetry. *J. Glaciol.* 54 (188), 778–787. <http://dx.doi.org/10.3189/002214308787780067>.
- Armstrong, R.L., Brun, E., 2008. *Snow and Climate: Physical Processes, Surface Energy Exchange and Modeling*. Cambridge University Press, ISBN: 9780521854542, URL <https://books.google.ca/books?id=7zZZi77gArMC>.
- Ashokkumar, L., Hari, C., 2020. 21st century estimates of mass loss rates from glaciers in the Gulf of Alaska and Canadian Archipelago using a GRACE constrained glacier model. *Cryosphere Discuss.* 2020, 1–32. <http://dx.doi.org/10.5194/tc-2019-325>, URL <https://tc.copernicus.org/preprints/tc-2019-325/>.

- Aubry-Wake, Caroline, Pomeroy, John W., 2023. Predicting hydrological change in an Alpine glacierized basin and its sensitivity to landscape evolution and meteorological forcings. *Water Resour. Res.* 59 (9), e2022WR033363. <http://dx.doi.org/10.1029/2022WR033363>.
- Baghdadi, Nicolas, Zribi, Mehrez, 2016. Observation des surfaces continentales par Télédétection micro-onde: Techniques et méthodes. *Encyclopedia of Snow, Ice and Glaciers*, iSTE, ISBN: 978-1-78405-157-0, <http://dx.doi.org/10.51926/ISTE.9781784051570>.
- Başağaoğlu, Hakan, Chakraborty, Debaditya, Winterle, James, 2021. Reliable evapotranspiration predictions with a probabilistic machine learning framework. *Water* 13 (4), <http://dx.doi.org/10.3390/w13040557>.
- Baur, O., Kuhn, M., Featherstone, W.E., 2013. Continental mass change from GRACE over 2002–2011 and its impact on sea level. *J. Geod.* 87 (2), 117–125. <http://dx.doi.org/10.1007/s00190-012-0583-2>.
- Beamer, J.P., Hill, D.F., Arendt, A., Liston, G.E., 2016. High-resolution modeling of coastal freshwater discharge and glacier mass balance in the Gulf of Alaska watershed. *Water Resour. Res.* 52 (5), 3888–3909. <http://dx.doi.org/10.1002/2015WR018457>.
- Beck, H.E., McVicar, T.R., Vergopolan, N., Berg, A., Lutsko, N.J., Dufour, A., Zeng, Z., Jiang, X., van Dijk, A.I.J.M., Miralles, D.G., 2020. High-resolution (1 km) Köppen-Geiger maps for 1901–2099 based on constrained CMIP6 projections. *Sci. Data* 10, 724. <http://dx.doi.org/10.1038/s41597-023-02549-6>.
- Braithwaite, R.J., Raper, S.C.B., 2009. Estimating equilibrium-line altitude (ELA) from glacier inventory data. *Ann. Glaciol.* 50 (53), 127–132. <http://dx.doi.org/10.3189/172756410790595930>.
- Castellazzi, P., Burgess, D., Rivera, A., Huang, J., Longuevergne, L., Demuth, M.N., 2019. Glacial melt and potential impacts on water resources in the Canadian rocky mountains. *Water Resour. Res.* 55 (12), 10191–10217. <http://dx.doi.org/10.1029/2018WR024295>.
- Castellazzi, Pascal, Longuevergne, Laurent, Martel, Richard, Rivera, Alfonso, Brouard, Charles, Chaussard, Estelle, 2018. Quantitative mapping of groundwater depletion at the water management scale using a combined GRACE/InSAR approach. *Remote Sens. Environ.* 205, 408–418. <http://dx.doi.org/10.1016/j.rse.2017.11.025>.
- Chakraborty, D., Başağaoğlu, H., Gutierrez, L., Mirchi, A., 2021a. Explainable AI reveals new hydroclimatic insights for ecosystem-centric groundwater management. *Environ. Res. Lett.* 170, 114024. <http://dx.doi.org/10.1088/1748-9326/ac2fde>.
- Chakraborty, Debaditya, Başağaoğlu, Hakan, Winterle, James, 2021b. Interpretable vs. noninterpretable machine learning models for data-driven hydro-climatological process modeling. *Expert Syst. Appl.* 170, 114498. <http://dx.doi.org/10.1016/j.eswa.2020.114498>.
- Chakraborty, Debaditya, Ivan, Cristina, Amero, Paola, Khan, Maliha, Rodriguez-Aguayo, Cristian, Başağaoğlu, Hakan, Lopez-Berestein, Gabriel, 2021c. Explainable artificial intelligence reveals novel insight into tumor microenvironment conditions linked with better prognosis in patients with breast cancer. *Cancers* 13 (14), <http://dx.doi.org/10.3390/cancers13143450>.
- Chen, J.L., Tapley, B.D., Wilson, C.R., 2006. Alaskan mountain glacial melting observed by satellite gravimetry. *Earth Planet. Sci. Lett.* (ISSN: 0012-821X) 248 (1), 368–378. <http://dx.doi.org/10.1016/j.epsl.2006.05.039>.
- Chesnokova, A., Baraër, M., Laperrière-Robillard, T., Huh, K., 2020. Linking mountain glacier retreat and hydrological changes in southwestern yukon. *Water Resour. Res.* 56 (1), e2019WR025706. <http://dx.doi.org/10.1029/2019WR025706>, URL <https://agupubs.onlinelibrary.wiley.com/doi/abs/10.1029/2019WR025706>, e2019WR025706 2019WR025706.
- Ciabuschi, F., Venkateswaran, B., 2017. *Neural Networks with R: Smart Models Using CNN, RNN, Deep Learning, and Artificial Intelligence Principles*. Packt, Birmingham, UK Mumbai.
- Ciraci, Enrico, Velicogna, Isabella, Sutterley, Tyler Clark, 2018. Mass balance of Novaya Zemlya Archipelago, Russian High Arctic, using time-variable gravity from GRACE and altimetry data from ICESat and CryoSat-2. *Remote Sens.* 10 (11), <http://dx.doi.org/10.3390/rs10111817>.
- Ciraci, E., Velicogna, I., Swenson, S., 2020. Continuity of the mass loss of the world's glaciers and ice caps from the GRACE and GRACE Follow-On missions. *Geophys. Res. Lett.* 47 (9), e2019GL086926. <http://dx.doi.org/10.1029/2019GL086926>.
- Dikshit, Abhirup, Pradhan, Biswajeet, 2021. Interpretable and explainable AI (XAI) model for spatial drought prediction. *Sci. Total Environ.* 801, 149797. <http://dx.doi.org/10.1016/j.scitotenv.2021.149797>.
- Doumbia, C., Castellazzi, P., Rousseau, A.N., Amaya, M., 2020. High resolution mapping of ice mass loss in the gulf of Alaska from constrained forward modeling of GRACE data. *Front. Earth Sci.* 7, 360. <http://dx.doi.org/10.3389/feart.2019.00360>.
- Farinotti, Daniel, Longuevergne, Laurent, Moholdt, Geir, Duethmann, Doris, Mölg, Thomas, Bolch, Tobias, Vorogushyn, Sergiy, Güntner, Andreas, 2015. Substantial glacier mass loss in the Tien Shan over the past 50 years. *Nat. Geosci.* 8 (9), 716–722. <http://dx.doi.org/10.1038/ngeo2513>.
- Farinotti, D., Longuevergne, L., Moholdt, G., Duethmann, D., Mölg, T., Bolch, T., Vorogushyn, S., Güntner, A., 2015. Substantial glacier mass loss in the Tien Shan over the past 50 years. *Nat. Geosci.* 8, 16–722. <http://dx.doi.org/10.1038/ngeo2513>.
- Fleming, Sean W., (Dan) Moore, R.D., Clarke, Garry K.C., 2006. Glacier-mediated streamflow teleconnections to the Arctic Oscillation. *Int. J. Climatol.* 26 (5), 619–636. <http://dx.doi.org/10.1002/joc.1273>, URL <https://rmetos.onlinelibrary.wiley.com/doi/abs/10.1002/joc.1273>.
- Fleming, Sean W., Whitfield, Paul H., 2010. Spatiotemporal mapping of ENSO and PDO surface meteorological signals in British Columbia, Yukon, and southeast Alaska. *Atmos.-Ocean* 48 (2), 122–131. <http://dx.doi.org/10.3137/AO1107.2010>.
- Foy, Norah, Copland, Luke, Zdanowicz, Christian, Demuth, Mike, Hopkinson, Chris, 2011. Recent volume and area changes of Kaskawulsh Glacier, Yukon, Canada. *J. Glaciol.* 57 (203), 515–525. <http://dx.doi.org/10.3189/002214311796905596>.
- Gardner, Alex S., Moholdt, Geir, Cogley, J. Graham, Wouters, Bert, Arendt, Anthony A., Wahr, John, Berthier, Etienne, Hock, Regine, Pfeffer, W. Tad, Kaser, Georg, Ligtenberg, Stefan R.M., Bolch, Tobias, Sharp, Martin J., Hagen, Jon Ove, van den Broeke, Michiel R., Paul, Frank, 2013. A reconciled estimate of glacier contributions to sea level rise: 2003 to 2009. *Science* 340 (6134), 852–857. <http://dx.doi.org/10.1126/science.1234532>.
- Gupta, Hoshin Vijai, Sorooshian, Soroosh, Yapo, Patrice Ogoou, 1999. Status of automatic calibration for hydrologic models: Comparison with multilevel expert calibration. *J. Hydrol. Eng.* 4 (2), 135–143. [http://dx.doi.org/10.1061/\(ASCE\)1084-0699\(1999\)4:2\(135\)](http://dx.doi.org/10.1061/(ASCE)1084-0699(1999)4:2(135)).
- Hartmann, Brian, Wendler, Gerd, 2005. The significance of the 1976 Pacific climate shift in the climatology of Alaska. *J. Clim.* 18 (22), 4824–4839. <http://dx.doi.org/10.1175/JCLI3532.1>, URL <https://journals.ametsoc.org/view/journals/clim/18/22/jcli3532.1.xml>.
- Hock, Regine, 2005. Glacier melt: a review of processes and their modelling. *Prog. Phys. Geogr.: Earth Environ.* 29 (3), 362–391.
- Hodge, Steven M., Trabant, Dennis C., Krimmel, Robert M., Heinrichs, Thomas A., March, Rod S., Josberger, Edward G., 1998. Climate variations and changes in mass of three glaciers in Western North America. *J. Clim.* 11 (9), 2161–2179. [http://dx.doi.org/10.1175/1520-0442\(1998\)011<2161:CVACIM>2.0.CO;2](http://dx.doi.org/10.1175/1520-0442(1998)011<2161:CVACIM>2.0.CO;2), URL https://journals.ametsoc.org/view/journals/clim/11/9/1520-0442_1998_011_2161_cvacim_2.0.co_2.xml.
- Huang, Qiwei, Ma, Ning, Wang, Ping, 2022. Faster increase in evapotranspiration in permafrost-dominated basins in the warming Pan-Arctic. *J. Hydrol.* 615, 128678. <http://dx.doi.org/10.1016/j.jhydrol.2022.128678>.
- Huang, Boyin, Thorne, Peter W., Banzon, Viva F., Boyer, Tim, Chepurin, Gennady, Lawrimore, Jay H., Menne, Matthew J., Smith, Thomas M., Vose, Russell S., Zhang, Huai-Min, 2017. Extended reconstructed sea surface temperature, version 5 (ERSSTv5): Upgrades, validations, and intercomparisons. *J. Clim.* 30 (20), 8179–8205. <http://dx.doi.org/10.1175/JCLI-D-16-0836.1>, URL <https://journals.ametsoc.org/view/journals/clim/30/20/jcli-d-16-0836.1.xml>.
- Hugonnet, Romain, McNabb, Robert W., Berthier, Etienne, Menounos, Brian, Nuth, Christopher, Girod, Luc, Farinotti, Daniel, Huss, Matthias, Dussailant, Inés, Brun, Fanny, Käib, Andreas, 2021. Accelerated global glacier mass loss in the early twenty-first century. *Nature* 592, 726–731, URL <https://api.semanticscholar.org/CorpusID:233446479>.
- Huss, Matthias, Hock, Regine, 2015. A new model for global glacier change and sea-level rise. *Front. Earth Sci.* 3, <http://dx.doi.org/10.3389/feart.2015.00054>.
- Huss, Matthias, Hock, Regine, 2018. Global-scale hydrological response to future glacier mass loss. *Nature Clim. Change* 8 (2), 135–140. <http://dx.doi.org/10.1038/s41558-017-0049-x>.
- Jakob, L., Gormelen, N., Ewart, M., Plummer, S., 2021. Spatially and temporally resolved ice loss in High Mountain Asia and the Gulf of Alaska observed by CryoSat-2 swath altimetry between 2010 and 2019. *Cryosphere* 15 (4), 1845–1862. <http://dx.doi.org/10.5194/tc-15-1845-2021>, URL <https://tc.copernicus.org/articles/15/1845/2021/>.
- Jin, Shuanggen, Zhang, T.Y., Zou, F., 2017. Glacial density and GIA in Alaska estimated from ICESat, GPS and GRACE measurements. *J. Geophys. Res.: Earth Surf.* 122 (1), 76–90. <http://dx.doi.org/10.1002/2016JF003926>.
- Josberger, Edward G., Bidlake, William R., March, Rod S., Kennedy, Ben W., 2007. Glacier mass-balance fluctuations in the Pacific Northwest and Alaska, USA. *Ann. Glaciol.* 46, 291–296. <http://dx.doi.org/10.3189/172756407782871314>.
- Kinnard, C., Larouche, O., Demuth, M.N., Menounos, B., 2022. Modelling glacier mass balance and climate sensitivity in the context of sparse observations: application to Saskatchewan Glacier, western Canada. *Cryosphere* 16 (8), 3071–3099. <http://dx.doi.org/10.5194/tc-16-3071-2022>.
- Koch, Johannes, Menounos, Brian, Clague, John J., 2009. Glacier change in Garibaldi Provincial Park, southern Coast Mountains, British Columbia, since the little ice age. *Glob. Planet. Change* (ISSN: 0921-8181) 66 (3), 161–178. <http://dx.doi.org/10.1016/j.gloplacha.2008.11.006>, URL <https://www.sciencedirect.com/science/article/pii/S0921818108001902>.
- Kochitzky, William, Dominic, Winski, Erin, McConnell, Karl, Kreutz, Seth, Campbell, Elynn M., Enderlin, Luke, Copland, Scott, Williamson, Brittany, Main, Hester, Jiskoot, 2020. Climate and surging of Donjek Glacier, Yukon, Canada. *Arct. Antarct. Alp. Res.* 52 (1), 264–280. <http://dx.doi.org/10.1080/15230430.2020.1744397>.
- Konz, Markus, Seibert, Jan, 2010. On the value of glacier mass balances for hydrological model calibration. *J. Hydrol.* 385 (1), 238–246. <http://dx.doi.org/10.1016/j.jhydrol.2010.02.025>.
- Larsen, C.F., Burgess, E., Arendt, A.A., O'Neel, S., Johnson, A.J., Kienholz, C., 2015. Surface melt dominates Alaska glacier mass balance. *Geophys. Res. Lett.* 42 (14), 5902–5908. <http://dx.doi.org/10.1002/2015GL064349>.

- LeDell, E., Poirier, S., 2020. H2O AutoML: Scalable automatic machine learning.
- Li, Yao-Jun, Ding, Yong-Jian, Shangguan, Dong-Hui, Wang, Rong-Jun, 2019. Regional differences in global glacier retreat from 1980 to 2015. *Adv. Clim. Change Res.* 10 (4), 203–213. <http://dx.doi.org/10.1016/j.accre.2020.03.003>.
- Li, Puleng, Kusche, Jürgen, Rietbroek, Roelof, Wang, Zhengtao, Forootan, Ehsan, Schulze, Kerstin, Lück, Christina, 2020. Comparison of data-driven techniques to reconstruct (1992–2002) and predict (2017–2018) GRACE-like gridded total water storage changes using climate inputs. *Water Resour. Res.* 56 (5), e2019WR026551. <http://dx.doi.org/10.1029/2019WR026551>.
- Lundberg, Scott M., Erion, Gabriel G., Chen, Hugh, DeGrave, Alex J., Prutkin, Jordan M., Nair, Bala G., Katz, Ronit, Himmelfarb, Jonathan, Bansal, Nisha, Lee, Su-In, 2019. Explainable AI for trees: From local explanations to global understanding. *ArXiv abs/1905.04610*, URL <https://api.semanticscholar.org/CorpusID:152282481>.
- Lundberg, S.M., Erion, G., Chen, H., DeGrave, A., Prutkin, J.M., Nair, B., Katz, R., Himmelfarb, J., Bansal, N., Lee, S.-I., 2020. From local explanations to global understanding with explainable AI for trees. *Nat. Mach. Intell.* 2, 56–67. <http://dx.doi.org/10.1038/s42256-019-0138-9>.
- Luthcke, Scott B., Arendt, Anthony A., Rowlands, David D., McCarthy, John J., Larsen, Christopher F., 2008. Recent glacier mass changes in the Gulf of Alaska region from GRACE mascon solutions. *J. Glaciol.* 54 (188), 767–777. <http://dx.doi.org/10.3189/002214308787779933>.
- Marshall, S.J., Miller, K., 2020. Seasonal and interannual variability of melt-season albedo at Haig Glacier, Canadian Rocky Mountains. *Cryosphere* 14 (10), 3249–3267. <http://dx.doi.org/10.5194/tc-14-3249-2020>, URL <https://tc.copernicus.org/articles/14/3249/2020/>.
- Mölg, Thomas, Maussion, Fabien, Scherer, Dieter, 2014. Mid-latitude westerlies as a driver of glacier variability in monsoonal high Asia. *Nature Clim. Change* 4, 68–73. <http://dx.doi.org/10.1038/nclimate2055>.
- Molnia, B.F., 2008. *Glaciers of North America - Glaciers of Alaska, Satellite Image Atlas of Glaciers of the World*. United States Gov. Print. Off, Washington, DC.
- Muñoz, S.J., 2019. ERA5-Land monthly averaged data from 1981 to present.
- Nash, J.E., Sutcliffe, J.V., 1970. River flow forecasting through conceptual models part I — A discussion of principles. *J. Hydrol.* 10 (3), 282–290. [http://dx.doi.org/10.1016/0022-1694\(70\)90255-6](http://dx.doi.org/10.1016/0022-1694(70)90255-6).
- Neal, E.G., Todd Walter, M., Coffeen, C., 2002. Linking the pacific decadal oscillation to seasonal stream discharge patterns in Southeast Alaska. *J. Hydrol.* (ISSN: 0022-1694) 263 (1), 188–197. [http://dx.doi.org/10.1016/S0022-1694\(02\)00058-6](http://dx.doi.org/10.1016/S0022-1694(02)00058-6), URL <https://www.sciencedirect.com/science/article/pii/S0022169402000586>.
- Oerlemans, J., 2005. Extracting a climate signal from 169 glacier records. *Science* 308 (5722), 675–677. <http://dx.doi.org/10.1126/science.1107046>, URL <https://www.science.org/doi/abs/10.1126/science.1107046>.
- Pancotto, Francesca, Addessi, Giorgio, Auteri, Nicola, 2024. Soccer bubble: Is there a speculative bubble in the price of international soccer players? *J. Sports Econ.* 25 (5), 535–556. <http://dx.doi.org/10.1177/15270025241239631>.
- Radić, Valentina, Bliss, Andrew, Beedlow, A. Cody, Hock, Regine, Miles, Evan, Cogley, J. Graham, 2014. Regional and global projections of twenty-first century glacier mass changes in response to climate scenarios from global climate models. *Clim. Dyn.* 42 (1–2), 37–58. <http://dx.doi.org/10.1007/s00382-013-1719-7>.
- RGI Consortium, 2017. *Randolph glacier inventory - A dataset of global glacier outlines, version 6 01 RGI60 Alaska*.
- Ribeiro, Marco Tulio, Singh, Sameer, Guestrin, Carlos, 2016. “Why should I trust you?": Explaining the predictions of any classifier.
- Rounce, David R., Hock, Regine, Shean, David E., 2020. Glacier mass change in High Mountain Asia through 2100 using the open-source python glacier evolution model (PyGEM). *Front. Earth Sci.* 7, <http://dx.doi.org/10.3389/feart.2019.00331>.
- Rousseau, A.N., Savary, S., Tremblay, S., Caillouet, L., Doumbia, C., Augas, J., Foulon, E., Abbasnezhadi, K., 2020. A Distributed Hydrological Modelling System to Support Hydroelectric Production in Northern Environments under Current and Changing Climate Conditions (No. R1926). Centre Eau Terre Environnement Institut national de la recherche scientifique (INRS-ETE) 490, rue de la Couronne, Québec (QC), G1K 9A9.
- Roy, Nita, Sen, Indira S., Boral, Soumita, Shukla, Tanuj, Velu, Vinoj, 2024. Isotope hydrograph separation reveals rainfall on the glaciers will enhance ice meltwater discharge to the Himalayan Rivers. *Water Resour. Res.* 60 (6), e2023WR034528. <http://dx.doi.org/10.1029/2023WR034528>, URL <https://agupubs.onlinelibrary.wiley.com/doi/abs/10.1029/2023WR034528>, e2023WR034528 2023WR034528.
- Ryo, Masahiro, 2022. Explainable artificial intelligence and interpretable machine learning for agricultural data analysis. *Artif. Intell. Agric.* (ISSN: 2589-7217) 6, 257–265. <http://dx.doi.org/10.1016/j.aiia.2022.11.003>, URL <https://www.sciencedirect.com/science/article/pii/S2589721722000216>.
- Samuel, J., Kavanaugh, B., Benkert, B., Samolczyck, M., Samolczyck, S., Evans, R., Saal, S., Gonet, J., Horton, B., Clague, J., Harmer, Z., Kinnear, L.P.H., 2016. Evaluating Climate Change Impacts on the Upper Yukon River Basin: Projecting Future Conditions Using Glacier, Climate and Hydrological Models. Northern Climate Exchange, Yukon Research Centre, Whitehorse, Yukon.
- Save, Himanshu, 2020. CSR GRACE and GRACE-FO RL06 mascon solutions v02.
- Save, Himanshu, Bettadpur, Srinivas, Tapley, Byron D., 2016. High-resolution CSR GRACE RL05 mascons. *J. Geophys. Res.: Solid Earth* 121 (10), 7547–7569. <http://dx.doi.org/10.1002/2016JB013007>.
- Scanlon, B.R., Zhang, Z., Rateb, A., Sun, A., Wiese, D., Save, H., Beaudoin, H., Lo, M.H., Müller-Schmied, H., Döll, P., van Beek, R., Swenson, S., Lawrence, D., Croteau, M., Reedy, R.C., 2019. Tracking seasonal fluctuations in land water storage using global models and GRACE satellites. *Geophys. Res. Lett.* 46 (10), 5254–5264. <http://dx.doi.org/10.1029/2018GL081836>.
- Shean, D.E., Bhushan, S., Montesano, P., Rounce, D.R., Arendt, A., Osmanoglu, B., 2020. Systematic, regional assessment of high mountain Asia glacier mass balance. *Front. Earth Sci.* 7, 363. <http://dx.doi.org/10.3389/feart.2019.00363>.
- Singh, V.P., Singh, P., Bishop, M.P., Björnsson, H., Haritashya, U.K., Haeberli, W., Oerlemans, J., Shroder, J.F., Tranter, M., 2011. *Encyclopedia of snow, ice and glaciers*. Encyclopedia of Snow, Ice and Glaciers, Springer Netherlands, ISBN: 9789048126415, URL <https://books.google.ca/books?id=mKktQR4T-1MC>.
- Stahl, K., Moore, R.D., Shea, J.M., Hutchinson, D., Cannon, A.J., 2008. Coupled modelling of glacier and streamflow response to future climate scenarios. *Water Resour. Res.* 44 (2), <http://dx.doi.org/10.1029/2007WR005956>.
- Stef, Nicolae, Başağaoğlu, Hakan, Chakraborty, Debadiitya, Ben Jabeur, Sami, 2023. Does institutional quality affect CO2 emissions? Evidence from explainable artificial intelligence models. *Energy Econ.* 124, 106822. <http://dx.doi.org/10.1016/j.eneco.2023.106822>.
- Sun, Zhangli, Long, Di, Yang, Wenting, Li, Xueying, Pan, Yun, 2020. Reconstruction of GRACE data on changes in total water storage over the global land surface and 60 basins. *Water Resour. Res.* 56 (4), e2019WR026250. <http://dx.doi.org/10.1029/2019WR026250>.
- Sun, Alexander Y., Scanlon, Bridget R., Save, Himanshu, Rateb, Ashraf, 2021. Reconstruction of GRACE total water storage through automated machine learning. *Water Resour. Res.* 57 (2), e2020WR028666. <http://dx.doi.org/10.1029/2020WR028666>.
- Tamisiea, M.E., Leuliette, E.W., Davis, J.L., Mitrovica, J.X., 2005. Constraining hydrological and cryospheric mass flux in southeastern Alaska using space-based gravity measurements. *Geophys. Res. Lett.* 32 (20), <http://dx.doi.org/10.1029/2005GL023961>.
- Vishwakarma, Bramha Dutt, Devaraju, Balaji, Sneeuw, Nico, 2018. What is the spatial resolution of grace satellite products for hydrology? *Remote Sens.* (ISSN: 2072-4292) 10 (6), <http://dx.doi.org/10.3390/rs10060852>, URL <https://www.mdpi.com/2072-4292/10/6/852>.
- Wahr, John, Burgess, Evan, Swenson, Sean, 2016. Using GRACE and climate model simulations to predict mass loss of Alaskan glaciers through 2100. *J. Glaciol.* 62 (234), 623–639. <http://dx.doi.org/10.1017/jog.2016.49>.
- Wang, Jon Y., Whitfield, Paul H., Cannon, Alex J., 2006. Influence of Pacific climate patterns on low-flows in British Columbia and Yukon, Canada. *Can. Water Resour. J. / Revue Canadienne Des Ressources Hydriques* 31 (1), 25–40. <http://dx.doi.org/10.4296/cwrj3101025>.
- Wang, Qiuyu, Yi, Shuang, Sun, Wenke, 2021. Continuous estimates of glacier mass balance in high mountain Asia based on ICESat-1,2 and GRACE/GRACE follow-on data. *Geophys. Res. Lett.* 48 (2), e2020GL090954. <http://dx.doi.org/10.1029/2020GL090954>, URL <https://agupubs.onlinelibrary.wiley.com/doi/abs/10.1029/2020GL090954>, e2020GL090954 2020GL090954.
- Wei, Linyong, Jiang, Shanhu, Ren, Liziang, Tan, Hongbing, Ta, Wanquan, Liu, Yi, Yang, Xiaoli, Zhang, Linqi, Duan, Zheng, 2021. Spatiotemporal changes of terrestrial water storage and possible causes in the closed Qaidam Basin, China using GRACE and GRACE follow-on data. *J. Hydrol.* (ISSN: 0022-1694) 598, 126274. <http://dx.doi.org/10.1016/j.jhydrol.2021.126274>.
- Wei, Xikun, Wang, Guojie, Grosser, Paula Farina, Schmalz, Britta, 2024. Using explainable artificial intelligence (XAI) methods to understand the nonlinear relationship between the Three Gorges Dam and downstream flood. *J. Hydrol.: Reg. Stud.* (ISSN: 2214-5818) 53, 101776. <http://dx.doi.org/10.1016/j.ejrh.2024.101776>, URL <https://www.sciencedirect.com/science/article/pii/S2214581824001241>.
- Yao, Tandong, Bolch, Tobias, Chen, Deliang, Gao, Jing, Immerzeel, W.W., Piao, Shilong, Su, Fengge, Thompson, Lonnie, Wada, Yoshihide, Wang, Lei, Wang, Tao, Wu, Guangjian, Xu, Baiqing, Yang, Wei, Zhang, Guoqing, Zhao, Ping, 2022. The imbalance of the Asian water tower. *Nat. Rev. Earth Environ.* 3, 1–15. <http://dx.doi.org/10.1038/s43017-022-00299-4>.
- Yao, Tandong, Thompson, Lonnie, Yang, Wei, Yu, Wusheng, Gao, Yang, Guo, Xuejun, Yang, Xiaoxin, Duan, Keqin, Zhao, Huabiao, Xu, Baiqing, Pu, Jiancheng, Lu, Anxin, Xiang, Yang, Kattel, Dambaru, Joswiak, Daniel, 2012. Different glacier status with atmospheric circulations in tibetan plateau and surroundings. *Nat. Clim. Change* 2, 663–667. <http://dx.doi.org/10.1038/nclimate1580>.
- Yu, Qitong, Wang, Shusen, He, Hongjie, Yang, Ke, Ma, Lingfei, Li, Jonathan, 2021. Reconstructing GRACE-like TWS anomalies for the Canadian landmass using deep learning and land surface model. *Int. J. Appl. Earth Obs. Geoinf.* 102, 102404. <http://dx.doi.org/10.1016/j.jag.2021.102404>.
- Zemp, M., Hoelzle, M., Haeberli, W., 2009. Six decades of glacier mass-balance observations: a review of the worldwide monitoring network. *Ann. Glaciol.* 50, 101–111. <http://dx.doi.org/10.1126/science.1072497>.

- Zemp, M., Huss, Matthias, Thibert, Emmanuel, Eckert, N., McNabb, Robert, Banwart, Jacqueline, Barandun, Martina, Machguth, Horst, Nussbaumer, Samuel, Gärtner-Roer, Isabelle, Thomson, L., Paul, Frank, Maussion, F., Kutuzov, Stanislav, Cogley, J., 2019. Global glacier mass changes and their contributions to sea-level rise from 1961 to 2016. *Nature* 568, <http://dx.doi.org/10.1038/s41586-019-1071-0>.
- Zhang, Z., Gu, Z., Hu, K., Hu, K., Xu, Y., Zhao, J., 2022. Spatial variability between glacier mass balance and environmental factors in the High Mountain Asia. *J. Arid Land* 14, 441–454. <http://dx.doi.org/10.1007/s40333-017-0014-z>.
- Zhi, W., Appling, A.P., Golden, H.E., Podgorski, J., Li, L., 2024. Deep learning for water quality. *Nat. Water* (ISSN: 0022-1694) 2, 228–241. <http://dx.doi.org/10.1038/s44221-024-00202-z>.
- Zhou, Jianmin, Li, Zhen, Fu, Xiyu, sen Tian, Bang, Huang, Lei, Chen, Quan, Zhang, Ping, Qiao, Dejing, 2019. Estimating the mass change of mountain glacier using a novel method based on InSAR observations. *Environ. Earth Sci.* 78, 1–9, URL <https://api.semanticscholar.org/CorpusID:133934150>.